Foreland-directed propagation of high-grade tectonism in the deep roots of a Paleoproterozoic collisional orogen, SW Montana, USA

Cailey B. Condit[1,*], Kevin H. Mahan[1], Alexis K. Ault[2], and Rebecca M. Flowers[1]
[1]DEPARTMENT OF GEOLOGICAL SCIENCES, UNIVERSITY OF COLORADO–BOULDER, 2200 COLORADO AVENUE, BOULDER, COLORADO 80309, USA
[2]DEPARTMENT OF GEOLOGY, UTAH STATE UNIVERSITY, 4505 OLD MAIN HILL, LOGAN, UTAH 84322, USA

ABSTRACT

The study of deeply exhumed ancient collisional belts offers important constraints on geologic processes and properties complementary to inaccessible portions of the crustal column in active orogens. The ca. 1.8–1.7 Ga Big Sky orogeny in southwest Montana is a major convergent belt associated with the Proterozoic amalgamation of Laurentia. New structural, petrologic, and geochronologic data from the Northern Madison Range, crossing the NE-SW trend of the belt, record key information about the internal dynamics of the orogen. At least two phases of Big Sky–related deformation are preserved, both nearly coeval with peak metamorphic conditions of ~0.9–0.8 GPa and >700 °C. Metamorphic zircon grains from a deformed mafic dike yield a weighted mean ion probe U-Pb date of 1737 ± 28 Ma (2σ). Monazite grains from a metapelite yield electron microprobe U-Th total-Pb dates of ca. 1750–1705 Ma, spanning prograde, peak, and retrograde intervals. Exposed Proterozoic paleodepths range from deeper levels (~45–40 km; 1.2 GPa) in the northwestern end of the range to shallower levels (~30–25 km) in the central-southeast area. The age of high-grade tectonism appears to become younger southeastward away from the core of the orogen, from ca. 1810–1780 Ma in the Highland Mountains, to ca. 1780–1750 Ma in the Ruby Range, Tobacco Root Mountains, and northwesternmost Northern Madison Range, and 1750–1720 Ma in the central Northern Madison Range. These spatial and temporal patterns of lateral growth and propagation of the orogen are similar to those observed in other collisional orogenic systems, and they may reflect multiple collision phases, protracted collision, and/or postcollisional collapse.

LITHOSPHERE; v. 7; no. 6; p. 625–645 | Published online 24 August 2015 doi:10.1130/L460.1

INTRODUCTION

Deeply eroded convergent belts offer exceptional natural laboratories in which to expand our understanding of crustal processes during continent formation. One such example is the recently recognized late Paleoproterozoic Big Sky orogen (e.g., O'Neill, 1998; Harms et al., 2004a), expressed as high-grade deep crust exposed within the Laramide basement-cored uplifts in southwest Montana, United States. Although a significant late Paleoproterozoic thermal disturbance was recognized along the northern margin of the Wyoming Province half a century ago (Giletti, 1966), it is only within the past 15 yr that substantial evidence emerged indicating that a significant collisional orogen transects central and southwest Montana (O'Neill, 1998; Mueller et al., 2002; Roberts et al., 2002; Berger et al., 2004; Harms et al., 2004a). However, major issues remain unresolved, including details of the scale and tempo of convergence, and how the internal dynamics of the Big Sky orogen evolved. Specific questions include the following. What is the along- and across-strike extent of the orogenic belt as defined by thermal and kinematic patterns, and what are the extents of the metamorphic core and foreland components? Can the timing of precollision convergence, initiation of collision, and duration of collision and postcollision relaxation processes be distinguished? These specific questions bear directly on larger questions regarding the assembly of Laurentia, including whether the rocks in southwest Montana represent one collision event or two (e.g., Mueller et al., 2005), or if there was any collision at all (Boerner et al., 1998).

New data are presented here from field and structural analysis, petrology, and geochronology in the Northern Madison Range, a key locality for clarifying the nature of the hinterland-foreland transition of the Big Sky orogen. Coupling high-spatial-resolution in situ geochronologic analysis of zircon and monazite with structural and petrologic observations allows recognition of links between accessory mineral growth, major phase reactions, and deformation textures. Results from this work show that Paleoproterozoic crustal depths of ≥25–30 km are exposed in the central portion of the Northern Madison Range, which considerably expands the across-strike extent of the orogen's metamorphic core. Moreover, the age of thermotectonism in the study area appears younger than in other parts of the region affected by the Big Sky orogeny, suggesting propagation of peak metamorphism and deformation from NW to SE over 40–80 m.y. These results are similar to lateral growth and propagation patterns observed in other major collisional orogens (e.g., Jamieson et al., 2011; Staples et al., 2014).

GEOLOGIC SETTING

Wyoming Province

The Wyoming Province is the southernmost component of the Archean core of North America and is bounded to the south, east, and northwest by Paleoproterozoic (ca. 1.8–1.7 Ga) orogenic belts (Cheyenne belt, Trans-Hudson orogen, and Paleoproterozoic component of the Great Falls tectonic zone, respectively; Gorman and Clowes, 2002; Mueller and Frost, 2006; O'Neill and Lopez, 1985). The northwestern part of the Wyoming Province is commonly referred to as the Montana metasedimentary province, one of several domains that are dis-

*cailey.condit@colorado.edu

tinguished based on lithology and general age (Mogk et al., 1992; Mueller et al., 2005; Foster et al., 2006). The Montana metasedimentary province includes most Precambrian crystalline exposures in southwest Montana and is approximately bounded to the southeast by Late Archean shear zones in the northwestern Beartooth Mountains (Fig. 1A). The province is characterized by a relative abundance of supracrustal metamorphic rocks, including pelitic schist, quartzite, and carbonate rocks along with ca. 3.3–3.0 Ga quartzofeldspathic gneiss and other granitoids (Mogk et al., 1992; Mueller et al., 1996). To the southeast, the Beartooth-Bighorn magmatic zone includes a larger proportion of 2.8 Ga orthogneiss and associated trondhjemite-tonalite-granodiorite suites (Mueller and Frost, 2006). The Precambrian rocks in southwest Montana have been tectonically reworked multiple times and metamorphosed to granulite and upper-amphibolite facies (e.g., Giletti, 1966; Spencer and Kozak, 1975; James and Hedge, 1980; Mogk, 1992; Harms et al., 2004a, 2004b). The dominant structural grain across the region strikes NE-SW, defined by major foliation and fold axial surfaces (e.g., Spencer and Kozak, 1975; Harms et al., 2004b), shear zones (e.g., Erslev and Sutter, 1990; Kellogg and Mogk, 2009; Johnson et al., 2014), and the overall trend of a thermochronologic feature called Giletti's line (defined in next paragraph; Giletti, 1966) and the Great Falls tectonic zone.

Early isotopic studies in the Montana metasedimentary province identified largely Archean protolith ages, but they also recognized a regional late Paleoproterozoic thermal overprint (Giletti, 1966, 1971; Mueller and Cordua, 1976; James and Hedge, 1980; Weyand, 1989; O'Neill et al., 1988; Mueller et al., 1993). Biotite and muscovite K-Ar and Rb-Sr dates are ca. 1.8–1.6 Ga northwest of a NE-trending transitional boundary that was originally drawn through the Southern and Northern Madison Ranges (Fig. 1B; Giletti, 1966, 1971; Reid et al., 1975; Mueller and Cordua, 1976). This feature, commonly referred to as "Giletti's line," was interpreted to represent the transition from warmer temperatures to the northwest, which induced complete resetting or new mica growth at 1.8–1.6 Ga, to cooler temperatures to the southeast, which were not high enough in Proterozoic time to significantly disturb the Ar system (Giletti, 1966). Subsequent work by Giletti (1971) revealed excess Ar in several biotite samples from the Gallatin Canyon localities, which called into question the exact position and nature of the thermal transition in the Northern Madison Range.

The spatial extent and magnitude of this late Paleoproterozoic thermotectonism remain unclear. Previous workers linked the Proterozoic thermal signature to relatively static low- to moderate-temperature overprinting, with associated localized greenschist-facies deformation, and assigned an Archean age to the regional upper-amphibolite- to granulite-facies tectonism (Mueller and Cordua, 1976; James and Hedge, 1980; Salt, 1987; Weyand, 1989; Erslev and Sutter, 1990; Mogk et al., 1992). More recent thermochronological (Harlan et al., 1996; Roberts et al., 2002; Brady et al., 2004a; Hames and Harms, 2013) and geochronological studies (Roberts et al., 2002; Mueller et al., 2004, 2005; Cheney et al., 2004; Ault et al., 2012; Alcock et al., 2013) documented high-grade metamorphism (up to granulite facies and 1.2 GPa) and deformation between ca. 1.8 and 1.7 Ga throughout the western ranges in the Montana metasedimentary province (Fig. 1). Harms et al. (2004a) called these tectonic events the Big Sky orogeny and suggested that they were caused by closure of an ocean basin and subsequent collision of the Archean Medicine Hat block with the Wyoming Province.

The extent of this overprint in the eastern part of the Montana metasedimentary province (Gravelly, Northern, and Southern Madison Ranges; Fig. 1B) is less certain. Much of the Northern Madison Range is located between the known Big Sky high-grade tectonism described here and a likely similarly aged, but localized Paleoproterozoic greenschist-facies shear zone, the Madison mylonite zone of Erslev and Sutter (1990), in the southern half of the Southern Madison Range (Fig. 1B). The low metamorphic grade of this shear zone and the apparent lack of warm Big Sky–aged temperatures (<300–400 °C) in much of the surrounding Southern Madison Range and Gravelly Range suggest that these ranges represent the Big Sky foreland. Consequently, the Northern Madison Range is an important area in which to further clarify the nature and location of the hinterland-foreland transition of the Big Sky orogen.

Northern Madison Range

The Northern Madison Range (Fig. 2) is an ~50-km-long, NW-SE–trending, Laramide-age, basement-cored uplift bounded to the south by the steeply dipping Spanish Peaks thrust fault (Garihan et al., 1983), which was last active during the Late Cretaceous (Kellogg and Harlan, 2007). The core of the range is predominantly Archean crystalline rock that has been multiply deformed and metamorphosed (Spencer and Kozak, 1975; Kellogg and Mogk, 2009). Recent work indicates that at least the northwest portion of the range shows evidence for Paleoproterozoic Big Sky tectonometamorphism (Ault et al., 2012).

Lithologies and Tectonic Interpretations

The range consists of quartzofeldspathic orthogneiss, foliated granitoids, mafic amphibolite, supracrustal schist, and quartzite. Previous workers distinguished two separate terranes based on variations in lithologies and metamorphic assemblages (Salt, 1987; Weyand, 1989; Mogk et al., 1992). The Jerome Rocks Lake terrane contains predominantly trondhjemitic gneiss, sillimanite-bearing metapelite and migmatite, and it is separated by the Mirror Lake shear zone from orthogneiss with intercalated kyanite- and sillimanite-bearing metapelitic schist, quartzite, ultramafic schist, and amphibolite of the Gallatin Peak terrane to the south (Salt, 1987;Fig. 2). Salt (1987) and Mogk et al. (1992) interpreted the Gallatin Peak terrane as representing a ca. 3.2 Ga subduction-related calc-alkaline continental magmatic arc. U-Pb zircon dates from orthogneiss units in both terranes yielded a range of ca. 3.3–2.7 Ga crystallization ages (Weyand, 1989).

Structural Grain and High-Strain Zones

The dominant structural trend is a NE-SW–striking foliation that varies considerably in dip magnitude and direction, and that ranges in intensity, with several high-strain zones that are locally mylonitic. Spencer and Kozak (1975) interpreted two main stages of deformation in the range: (1) early gneissic foliation development and isoclinal folding of the foliation, and (2) subsequent ductile deformation and the development of broad folds. Discrete high-strain zones include the Mirror Lake and Big Brother shear zones (Salt, 1987; Mogk and Henry, 1988; Mogk et al., 1992), Crooked Creek mylonite (Kellogg and Mogk, 2009), the Hellroaring Creek shear zone, and the Spanish Creek mylonite (Johnson et al., 2014; Fig. 2). These ductile shear zones generally strike NE-SW and dip moderately to steeply to the SE or NW (Fig. 2). The timing of this deformation is not well constrained. Previous studies suggested a Late Archean age for the Mirror Lake shear zone and Crooked Creek mylonite (Weyand, 1989; Mogk et al., 1992; Kellogg and Mogk, 2009). However, the prevalence and proximity of Proterozoic high-grade metamorphism and deformation in nearby ranges to the south and west (e.g., Erslev and Sutter, 1990; Harms et al., 2004b) coupled with new data from this study suggest that some of the deformation is likely Paleoproterozoic.

Patterns and Timing of Metamorphism

The metamorphic grade observed within the Northern Madison Range varies from granulite to amphibolite facies (Spencer and Kozak, 1975; Salt, 1987; Mogk and Henry, 1988; Ault et al., 2012), with some greenschist-facies overprint-

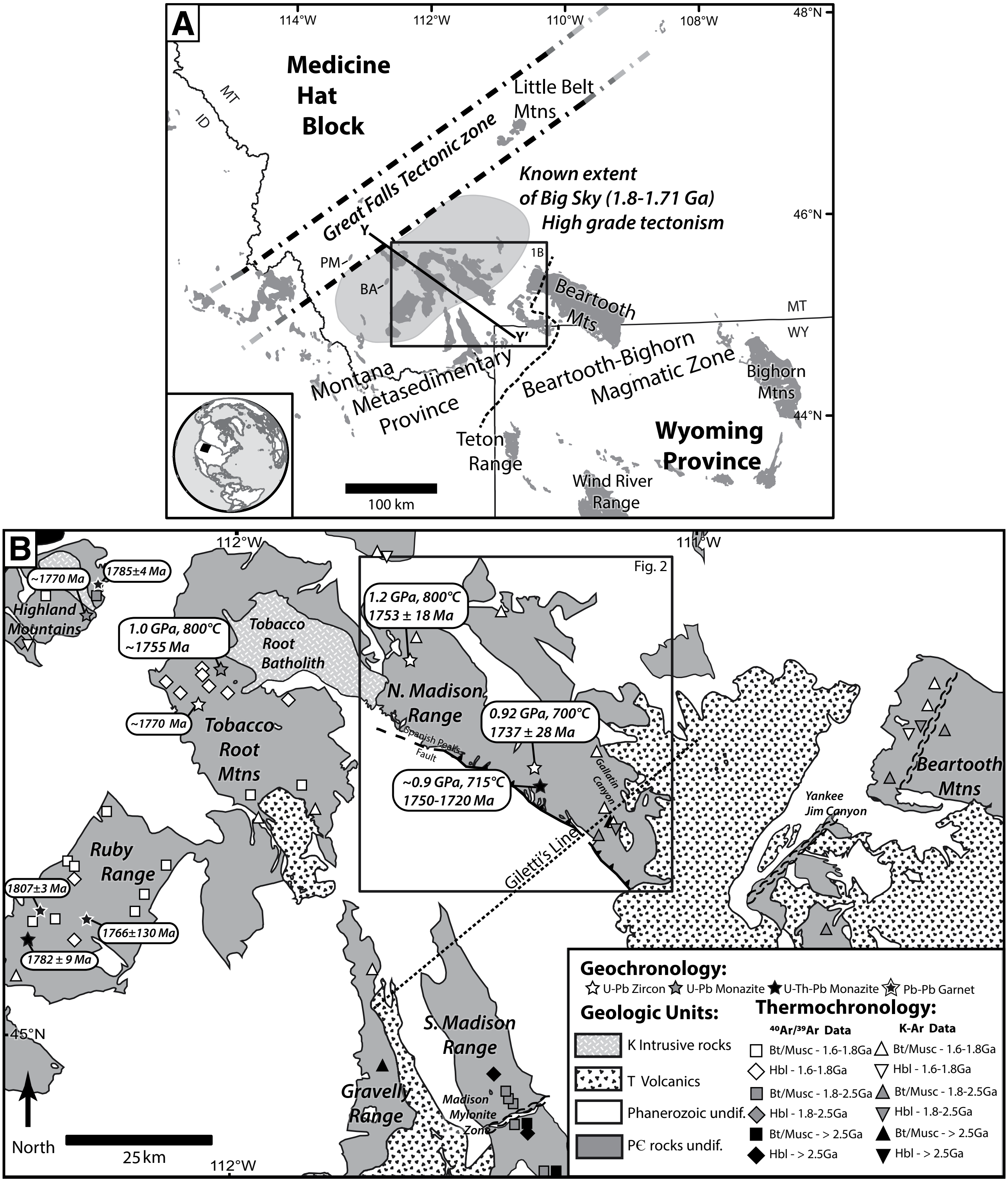

Figure 1. (A) Regional map showing northwest margin of Wyoming Province, location of Great Falls tectonic zone, the Medicine Hat block, and the known extent of the Big Sky orogen (light-gray shading). Basement-cored uplifts exposing Precambrian rocks are shown in dark gray. PM—Pioneer Mountains; BA—Biltmore anticline; thin dashed line—boundary between the Montana metasedimentary province and the Beartooth-Bighorn magmatic zone; MT—Montana; ID—Idaho; WY—Wyoming. (B) Simplified geologic map of southwest Montana showing the location of major basement-cored uplifts, Cretaceous intrusive rocks, and Tertiary volcanics. Also shown are published K-Ar thermochronology data (Giletti, 1966, 1971; Reid et al., 1975), $^{40}Ar/^{39}Ar$ thermochronology data (Erslev and Sutter, 1990; Harlan et al., 1996; Roberts et al., 2002; Brady et al., 2004a; Hames and Harms, 2013), U-Pb zircon geochronology (Mueller et al., 2004; Ault et al., 2012; this study), U-Th-Pb monazite geochronology (Cheney et al., 2004a), U-Th-Pb monazite electron microprobe geochronology (Alcock et al., 2013; this study), Pb-Pb garnet geochronology (Roberts et al., 2002), and thermobarometry (Cheney et al., 2004b; Ault et al., 2012; this study). K—Cretaceous; T—Tertiary; PЄ—Precambrian. All mineral abbreviations are after Whitney and Evans (2010).

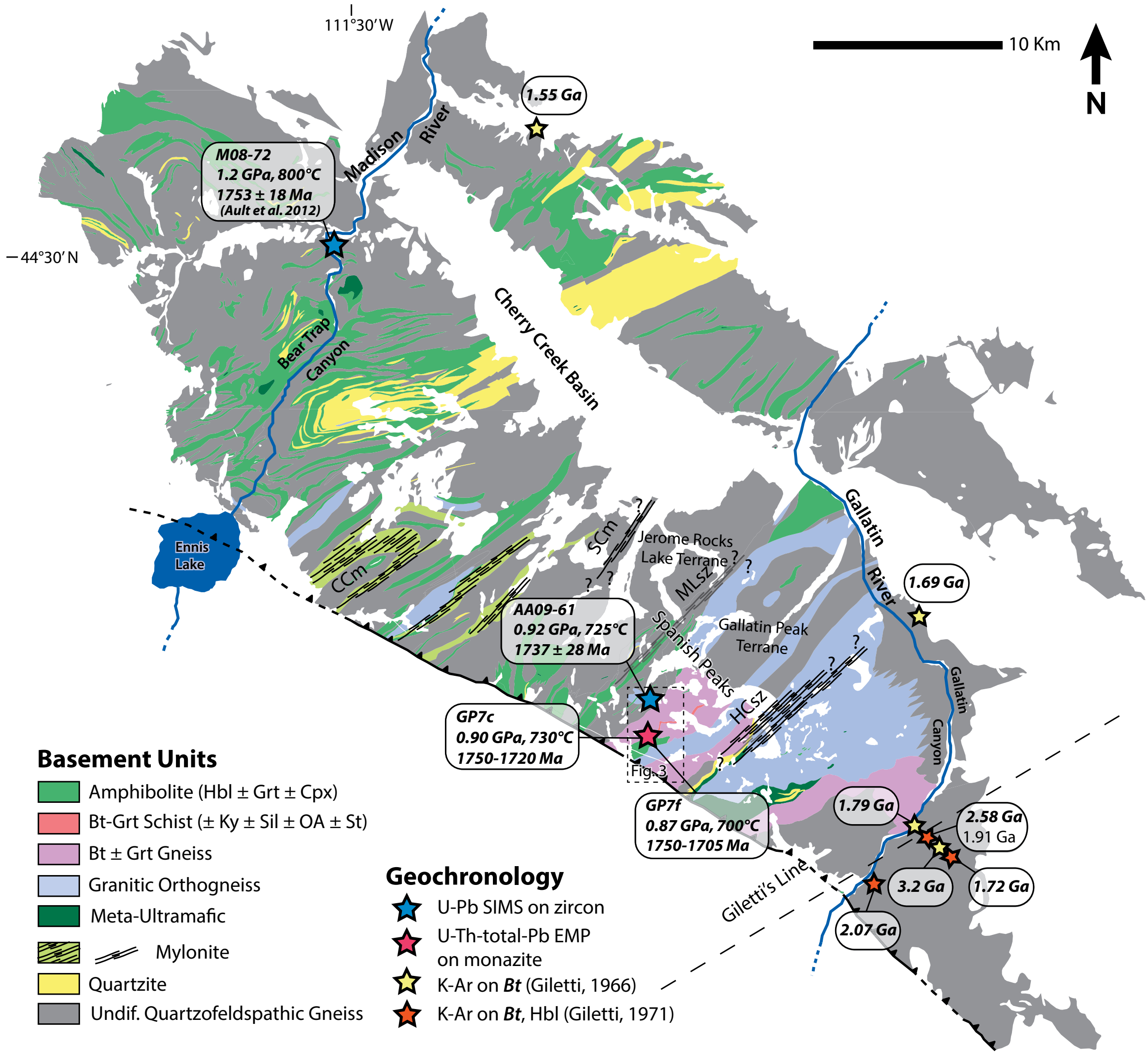

Figure 2. Simplified geologic map of the Northern Madison Range. U-Pb data and thermobarometry are from Ault et al. (2012) and this study, U-Th–total-Pb electron microprobe (EMP) data are from this study, K-Ar data are from Giletti (1966, 1971), and known high-strain zones are from Kellogg and Mogk, (2009), Johnson et al., (2014), Salt (1987), and this study. CCm—Crooked Creek mylonite, SCm—Spanish Creek mylonite, MLsz—Mirror Lake shear zone, HCsz—Hellroaring Creek shear zone; SIMS—secondary ion mass spectrometry. Map units are from Kellogg and Williams, (2000) and Vuke (2003). All mineral abbreviations are after Whitney and Evans (2010).

ing in the southeastern portion of the range in Gallatin Canyon (Condit et al., 2012). Previous thermobarometric estimates indicate relatively high pressure and temperature conditions of up to 1.0–0.7 GPa and up to 700 °C (Salt, 1987; Mogk and Henry, 1988; Kellogg and Mogk, 2009). The age of high-grade metamorphism was interpreted as Mesoarchean to Neoarchean (Mogk et al., 1992; Kellogg and Mogk, 2009; James and Hedge, 1980; Salt, 1987; Mueller and Frost, 2006). This interpretation is based on zircon crystallization ages for granitoids in the central part the Spanish Peaks area, interpreted to have been emplaced synchronously with metamorphism and deformation (Weyand, 1989). However, Ault et al. (2012) reported a 1753 ± 18 Ma metamorphic zircon age (ion probe, 2σ error) from a mafic dike that was metamorphosed and internally deformed at 1.2 GPa and 800 °C in the northwestern portion of the range (Fig. 2).

NORTHWEST GALLATIN PEAK TERRANE

This study is focused in Bear Basin and its surrounding areas, which occupy the northwest portion of the Gallatin Peak terrane (Figs. 2 and 3). Previous detailed work in this region is limited to theses by Salt (1987) and Weyand (1989) and a recently published map at 1:24,000 scale by Vuke (2013). Salt (1987) mapped the major lithologies in the Bear Basin region, and Weyand acquired multigrain U-Pb thermal ionization mass spectrometry (TIMS) zircon data from these units. For this study, the Bear Basin region was remapped at 1:15,000 with a focus on structural geology and key units for relative and absolute timing of deformation and metamorphism (Fig. 3).

Lithologies, Contact Relationships, and Previous Geochronology

The oldest known rocks in the Bear Basin region are a series of ca. 3.2–3.0 Ga granitoid

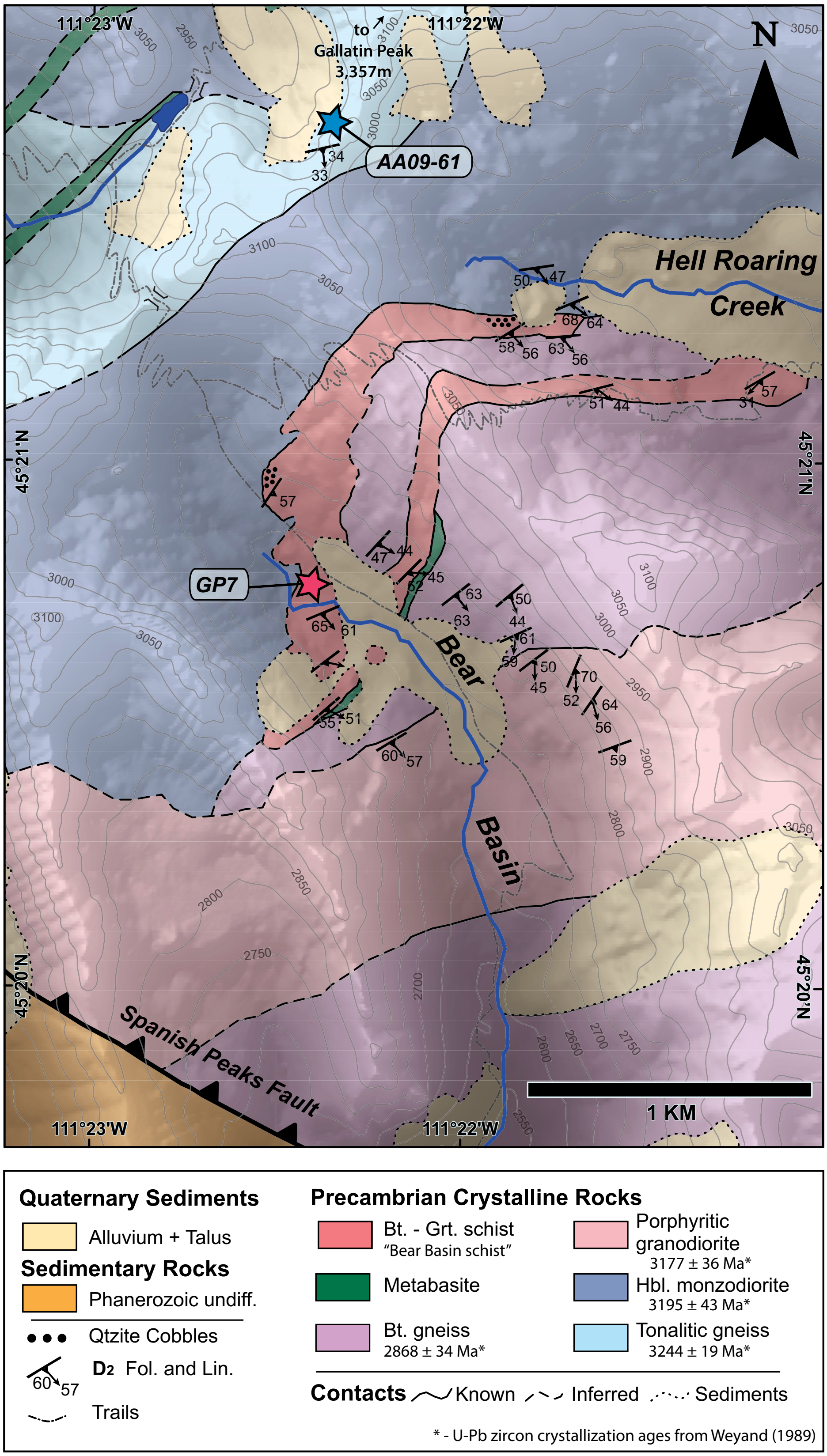

Figure 3. Simplified geologic map of the northwest Gallatin Peak terrane and Bear Basin area. Some map units are adapted from Kellogg and Williams (2000). U-Pb zircon geochronology is from Weyand (1989). Bt—biotite; Grt—garnet; Hbl—hornblende.

gneisses. The first major unit is a heterogeneous tonalitic gneiss with a zircon U-Pb crystallization age of 3244 ± 19 Ma (Weyand, 1989) that occurs in the vicinity of Gallatin Peak and south of the Mirror Lake shear zone. The unit consists of centimeter-scale layers of tonalite, diorite, and amphibolite, with variable proportions of Pl + Qz + Bt + Hbl (all mineral abbreviations after Whitney and Evans, 2010), and minor granitoid. South of the tonalitic gneiss exposures, a hornblende monzodiorite crops out (Fig. 3) that is similar to the tonalite in major mineralogy but is texturally more isotropic (non-layered), contains abundant millimeter-scale epidote, and yields a zircon U-Pb crystallization age of 3195 ± 43 Ma (Weyand, 1989). The third major unit is a porphyritic granodiorite exposed in the southern Bear Basin area (Fig. 3). It contains centimeter-scale relict K-feldspar phenocrysts and has a zircon U-Pb crystallization age of 3177 ± 36 Ma (Weyand, 1989). Salt (1987) documented inclusions of the previously described igneous units in this granodiorite and thus interpreted that the granodiorite is the youngest in the suite. Collectively, these units are the basis of Mogk et al.'s (1992) interpretation that the Gallatin Peak terrane represents part of a ca. 3.2 Ga calc-alkaline continental magmatic arc.

The fourth major unit is composed of intimately mixed and undifferentiated migmatitic biotite schist, granite, and granitic gneiss (Fig. 3, biotite gneiss unit). In the map area, this unit lacks sedimentary structures, and no aluminous metamorphic index minerals were observed other than local garnet. Weyand (1989) interpreted the protolith as igneous and reported a zircon U-Pb date of 2868 ± 24 Ma.

The youngest reported granitoid units within the Gallatin Peak terrane are small-volume foliated to unfoliated granites. Those we observed were 1–30-m-thick tabular sheets of Ms + Bt ± Grt leucogranite that are concordant with the foliated host rock. These leucogranites appear to be more abundant on the northern margin of the Hellroaring Creek shear zone (Fig. 2). Weyand (1989) reported a 2680 ± 130 Ma U-Pb zircon date for a weakly foliated granitic dike (Bt + Hbl + Ep + Pl) on the northern margin of the Gallatin Peak terrane.

Supracrustal rocks within the Gallatin Peak terrane include an intercalated package of aluminous schist, amphibolite, and minor quartzite. This unit crops out in central Bear Basin and in the adjacent upper drainage of Hellroaring Creek (Fig. 3). It is collectively referred to here as the Bear Basin schist. The schist contains a wide range of compositions, from aluminum-rich layers with varying amounts of kyanite (Fig. 4A), cordierite, sillimanite, staurolite, and garnet to less aluminous orthoamphibole-rich

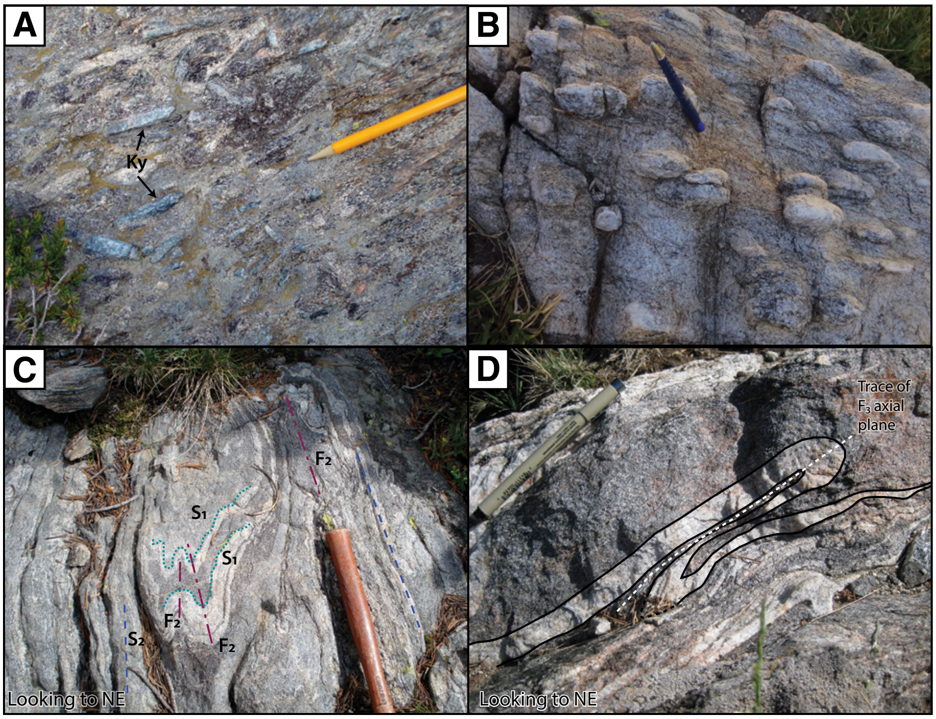

Figure 4. Field photographs and annotations of lithologies and structures in the northwest Gallatin Peak terrane. (A) Aluminous layer of Bear Basin schist containing large visible kyanite (Ky) crystals. (B) Quartzite cobble outcrop within the Bear Basin schist along NE contact with hornblende monzodiorite. (C) Relationship of transposed S_1 compositional layering to form limbs of F_2 folds that are parallel to S_2 axial planar surfaces within the Bear Basin schist. (D) Southeast-vergent Z-fold (F_3) of quartzofeldspathic layering within Bear Basin schist.

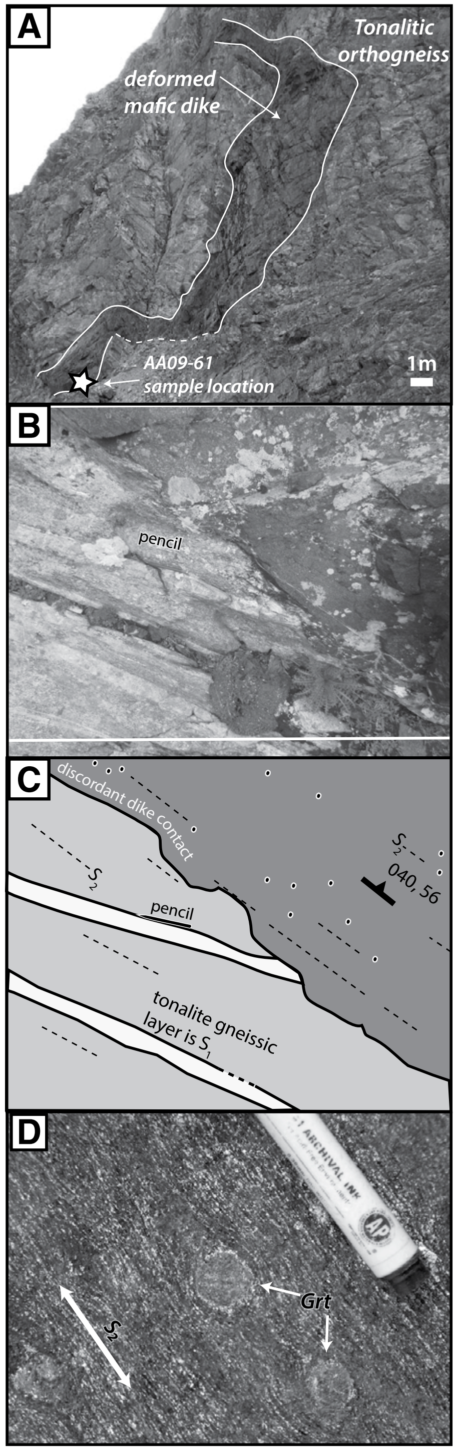

Figure 5. Deformed mafic dike from northwest Gallatin Peak terrane. (A) Field photograph of the dike intruding into tonalite gneiss, showing location of sample AA09-61. (B) Field photograph of discordant dike contact with tonalitic orthogneiss. (C) Corresponding sketch of the dike's discordant contact. (D) Hand sample photograph of garnet porphyroblasts surrounded by plagioclase haloes and pervasive S_2 fabric; Grt—garnet.

layers. Concordant garnet-hornblende amphibolite layers are interpreted as metavolcanics.

Salt (1987) interpreted a coarse Ged + Ky layer close to a contact with the Hbl-monzodiorite described in Bear Basin as a contact aureole, thus placing a minimum depositional age on the Bear Basin schist at ca. 3.2–3.1 Ga. However, the northwest contact between these two units is locally conglomeratic, with quartzite lenses and pebble-sized quartz and granitoid clasts (Fig. 4B) observed in at least two separate localities (Fig. 3). These observations suggest a depositional contact rather than an intrusive one, implying a maximum depositional age of ca. 3.1 Ga. Weyand (1989) also interpreted this unit as sedimentary in origin, based on whole-rock compositions, and implied that analyzed zircon, with $^{207}Pb/^{206}Pb$ dates ranging from 3025 to 3160 Ma, are detrital. This package is similar in lithology and appearance to the Spuhler Peak metamorphic suite found within the Tobacco Root Mountains, which has been interpreted to be a shallow-marine sequence of volcanics and intercalated sediments metamorphosed in a single event during the Big Sky orogeny (Burger et al., 2004).

Amphibolite dikes (Hbl + Pl ± Grt ± Cpx) appear to be some of the youngest intrusive units in the region (Fig. 5A), and they have similar deformational and crosscutting field relationships to the mafic dikes and sills observed in the Tobacco Root Mountains (Brady et al., 2004b) and in Bear Trap Canyon (Ault et al., 2012). The contacts of internally deformed dikes locally truncate early gneissic layering in tonalite units (Figs. 5B–5C). Although concordant amphibolite layers occur, no dikes with crosscutting contacts were observed in the Bear Basin schist, an observation similar to the Spuhler Peak metamorphic suite. Several undeformed postkinematic dikes thought to be late Proterozoic in age (Harlan et al., 1996) occur in the range, although none has been observed in the study area (Fig. 3).

Structural Geology

At least three phases of deformation affected the rocks of the Gallatin Peak terrane (Table 1). The earliest structures likely represent more than one phase of deformation. These include early gneissic layering in the tonalite, early penetrative foliation in the Bear Basin schist, magmatic layering defined by variable concentrations of K-feldspar phenocrysts in the porphyritic granodiorite, and locally preserved inclusion

TABLE 1. DEFORMATION PHASES AND ASSOCIATED STRUCTURES

Associated structures	Description	Mean orientations
D$_1$		
S$_{1\ gneiss}$	Transposed compositional layer within tonalitic gneiss and truncated by deformed mafic dikes.	Transposed S$_1$ + S$_2$
S$_{1\ schist}$	Transposed compositional layering within Bear Basin schist.	
S$_{1\ inclusion}$	Inclusion trail pattern within garnet porphyroblasts in deformed mafic dikes that truncate S$_{1\ gneiss}$.	
D$_2$		
S$_2$	NE-SW–striking foliation surfaces that moderately dip to the SE.	044°, 57°
F$_2$	Open to tight folds of local S$_1$ foliation fabrics. Hinge line subparallel to L$_2$ lineations.	Axial plane: 041°, 68°; hinge line: 70° → 105°
L$_2$	Mineral lineations on S$_2$ surfaces.	60° → 129°
D$_3$		
F$_3$	Steeply inclined, moderately plunging SE-vergent Z-folds of S$_2$ fabrics.	Axial plane: 001°, 68° Hinge line: 54° → 152°

trails within porphyroblastic garnet in deformed mafic dikes. Our observations indicate that these earliest fabrics cannot all be the same age. For instance, the gneissic layering in the tonalite is locally truncated by intrusive contacts of the deformed and metamorphosed mafic dikes (Figs. 5B–5C). However, for the purposes of this paper, all of these structures are collectively referred to as D$_1$, and all are variably transposed by D$_2$ structures (e.g., Fig. 4C). The early structures are locally preserved in low-strain regions such as the hinge of a map-scale F$_2$ fold in Bear Basin or in other low-strain zones in the upper drainage of Hellroaring Creek (Fig. 3). There, S$_1$ and F$_2$ enveloping surfaces tend to strike N or NW with moderate to steep dips, and they are distributed in a manner that is consistent with variable reorientation by later F$_2$ and probably F$_3$ folding (Fig. 6A).

D$_2$ deformation is the most pervasive in the range, and D$_2$ structures are ubiquitous within the rocks of the northern portion of the Gallatin Peak terrane. The penetrative S$_2$ foliation is NE striking and moderately SE dipping, with a mean orientation of 044°, 57° (Fig. 6B). S$_2$ surfaces contain a mineral lineation (L$_2$) defined by biotite, hornblende, or kyanite and/or a stretching lineation defined primarily by elongate feldspar grains or locally by stretched pebbles in conglomeratic horizons of the Bear Basin schist. L$_2$ has a mean orientation that is approximately downdip (60°→129°; Fig. 6B). F$_2$ folds are common and recognizable from outcrop to kilometer scales. These folds are tight to isoclinal (Fig. 4C), with axial surfaces subparallel to S$_2$ and with hinge lines that are subparallel to L$_2$ (Fig. 6C). The one exception is in a relatively low D$_2$ strain zone in the upper drainage of Hellroaring Creek, where F$_2$ hinge lines consistently plunge N to NE, possibly reflecting regional variability in the pre-D$_2$ orientation of the folded S$_1$ surfaces or that D$_2$ strain was not sufficiently high enough in this area to rotate the F$_2$ hinge lines to the direction of maximum stretching. The most prominent map-scale D$_2$ structure is a kilometer-scale, moderately inclined, and moderately southeast-plunging synformal isoclinal fold of the Bear Basin schist (Fig. 3). The hinge region of this fold is exposed in central Bear Basin (Fig. 4C).

The youngest deformation phase observed in the region (D$_3$) is limited to steeply inclined and moderately plunging, open to tight folds of the S$_2$ fabric (Fig. 4D). The mean axial surface of F$_3$ folds (001°, 68°) strikes more northerly than that of F$_2$ folds, but hinge line orientations are similar (mean trend and plunge 54°®152°). F$_3$ structures commonly have NE-vergent Z-asymmetry (Fig. 6C).

The Gallatin Peak terrane is bounded to the northwest by the Mirror Lake shear zone, described by Salt (1987) as an ~500-m-wide, NE-striking, and moderately SE-dipping shear zone. We have not observed this structure, and it is not exposed in the study area. A second high-strain zone, here named the Hellroaring Creek shear zone, forms the approximate southeastern boundary of the study area (Fig. 2). This

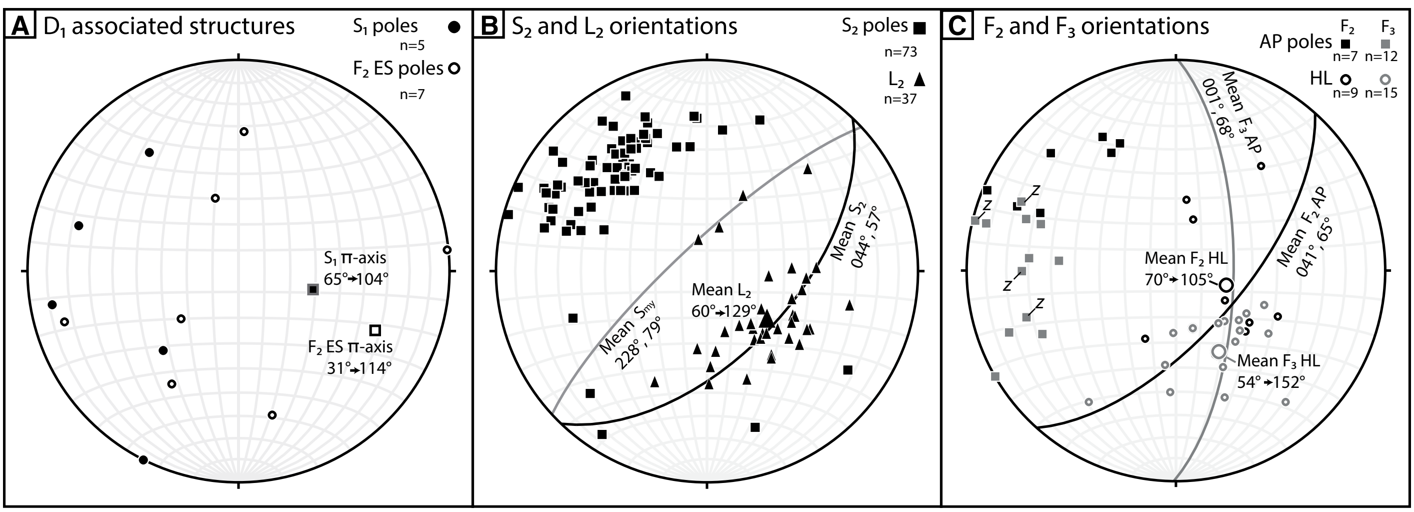

Figure 6. Lower-hemisphere stereographic projection of major structures within the northwest Gallatin Peak terrane. (A) Poles and π-axis to both S$_1$ layering and enveloping surfaces of F$_2$ folds. (B) Poles to S$_2$ foliation fabric, lines of L$_2$ mineral lineations, and mean S$_2$ and L$_2$ orientations. S$_{my}$ is the mean mylonitic foliation plane of the Hellroaring Creek shear zone. (C) Axial planar poles, hinge lines, and mean orientations for F$_2$ and F$_3$ folds. "z" designates a Z-fold. ES—enveloping surface, AP—axial plane, HL—hinge line.

structure is a 1.5–2-km-wide zone of strongly foliated to mylonitic rocks that strikes southwest and dips steeply to the northwest (mean orientation 228°, 79°; Fig. 6B). Shear sense indicators record components of SE-vergent thrust displacement and right-lateral shearing, suggesting a transpressional environment. The dextral and reverse asymmetry of F_3 folds described here suggests that these folds may be a coeval and lower-strain expression of the Hellroaring Creek shear zone.

D_1 and D_2 structures described here both belong to the "first orogeny" of the more regional study by Spencer and Kozak (1975). Their "second orogeny" was based on the observation that the dominant foliation across the range varies in dip direction from SE to NW, and thus large-scale folds without an associated axial planar foliation were inferred. In the present study area, similar variation in the orientation of dominant penetrative fabrics is explained by overprinting of the S_2 foliation by the Hellroaring Creek shear zone in the eastern portion of the study area, which is tentatively related to D_3. Salt (1987) recognized two sets of fold styles in this region that appear to correlate with F_2 and F_3 as described here. It was concluded from that study that both fold sets formed at relatively high temperature, and thus probably developed close in time during one orogenic cycle.

PETROLOGY AND GEOCHRONOLOGY

Sample Targets, Descriptions, and Textures

Two samples of Bear Basin schist (GP7c and GP7f) and one mafic dike sample (AA09-61) were targeted to help constrain conditions and timing of metamorphism and deformation in the Gallatin Peak terrane. The Bear Basin schist was sampled in a pelitic horizon because the mineral assemblages are amenable to quantitative thermobarometry and monazite geochronology. The mafic dikes were targeted because they represent the youngest metamorphosed and deformed intrusive units in the study area. Pressure and temperature (*P-T*) equilibrium conditions calculated from all three samples constrain representative metamorphic conditions in the northwest portion of the Gallatin Peak terrane. Geochronology included electron microprobe (EMP) U-Th–total Pb analysis of monazite from the two Bear Basin schist samples and in situ secondary ion mass spectrometry (SIMS) U-Pb zircon dating of the mafic dike sample.

The two Bear Basin schist samples were collected near the hinge region of the kilometer-scale F_2 fold in Bear Basin (Fig. 3). Sample GP7c is from an ~1–2-m-thick layer and contains Grt + Ky + Sil + St + Bt + Pl + Qz, with accessory zircon, monazite, and xenotime. The sample contains a dominant S_2 fabric, which is defined by (1) shape-preferred orientations of biotite, staurolite, kyanite, and sillimanite, and (2) alternating millimeter- to centimeter-scale layers of Pl + Bt + Qz and more aluminous layers. Sample GP7f, located several meters away, exhibits an S_1 fabric only partially transposed by F_2 folds. The sample is from a less-aluminous component of the schist, containing Grt + Bt + Pl + Qz and accessory monazite, zircon, and rutile. The GP7f thin section was cut perpendicular to the F_2 hinge line, so that traces of S_1 and S_2, both defined primarily by aligned biotite, are visible.

Garnet porphyroblasts in both Bear Basin schist samples are 0.5–3 mm in diameter, are subhedral to anhedral, and contain abundant inclusions of biotite, quartz, monazite, zircon, and fracture-filling late chlorite (Figs. 7A–7B). Kyanite is also locally included in garnet in sample GP7c (Fig. 7A), suggesting that it was the first aluminosilicate to stabilize. Both kyanite and sillimanite occur in the matrix as fabric-defining phases, with sillimanite texturally appearing to form after kyanite, (Fig. 7C). Although staurolite occurs in the matrix of sample GP7c (Fig. 7D), it is locally restricted as inclusions in garnet in other samples from the same outcrop (Fig. 7E), implying growth as an early prograde phase. As described in detail here, monazite occurs throughout the matrix in both schist samples and commonly as inclusions in several of the major mineral phases (Figs. 7A–7E). Xenotime was observed as an inclusion in staurolite (Fig. 7E), but not in the matrix in GP7c, and the phase was not observed in GP7f.

Sample AA09-61 was collected from an amphibolite dike that crops out on the flank of Gallatin Peak, ~1 km north of Bear Basin (Fig. 3). Dike contacts are locally discordant to an early gneissic layering in the tonalite host (S_1 gneiss, Figs. 5B–5C). The dike contains a dominant penetrative S_2 fabric, defined by aligned hornblende and plagioclase, that appears axial planar to a meter-scale F_2 fold of the dike and host gneiss (Fig. 5A). The sample contains Hbl + Pl + Qz + Ilm ± Bt with ~15–10-mm-diameter anhedral to subhedral garnet porphyroblasts (Figs. 5D and 7F). Garnet porphyroblasts contain abundant inclusions of hornblende, plagioclase, quartz, biotite, and ilmenite that define an earlier fabric oblique to the penetrative foliation within the dike. Garnet porphyroblasts are mantled by inner plagioclase and outer hornblende haloes. Plagioclase in the inner halo is evenly distributed around the garnet, whereas the outer hornblende haloes are commonly elongate in the S_2 fabric. Euhedral hornblende locally occurs within the plagioclase halo.

Mineral Compositions

Elemental X-ray maps for Ca, Al, Mg, and Mn and mineral compositions were analyzed using a JEOL 8600 electron microprobe at the University of Colorado–Boulder. Beam conditions of 15 kV voltage, 50 nA current, 100 µs dwell time, and step size of ~10–25 µm were used for X-ray maps. Quantitative mineral compositions were acquired with 15 kV voltage, 20 nA current, and a focused beam (~1 µm diameter) for garnet and staurolite, and defocused beam (5–10 µm diameter) for micas, amphiboles, and feldspars, and count times ranging from 20 to 40 s. Select mineral compositions are reported in Table 2, and those used in thermobarometry calculations are noted.

GP7c and GP7f

Garnet compositions in both samples are dominantly almandine (X_{Alm} = 0.62–0.66 in GP7c; 0.72–0.76 in GP7f). Magnesium number (Mg#) is broadly homogeneous in the cores (0.30 in GP7c; 0.24 in GP7f) and sharply drops near the rims (0.24 in GP7c; 0.20 in GP7f). Spessartine content is also homogeneous in grain interiors, with a slight increase at the rim (from 0.09 to 0.11 in GP7c; 0.01 to 0.04 in GP7f), especially in smaller, isolated garnet islands (Figs. 8A–8B). Grossular garnet composition in sample GP7c is very low (X_{Grs} = 0.01), and the garnet is unzoned with respect to Ca. Calcium in garnet in sample GP7f is slightly zoned, with the core recording X_{Grs} = 0.04, a drop to 0.03 in a distinct moat, and an increase to 0.04 along the rims (Fig. 8B). These garnet compositional patterns suggest homogenization at high temperature with late modifications associated with limited resorption (X_{Sps} increase at margins) and diffusional Mg-Fe exchange (Tracy et al., 1976; Kohn and Spear, 2000).

Biotite is unzoned in both samples (Mg# = 0.60–0.62 in GP7c; 0.53–0.55 in GP7f). Staurolite in GP7c has Mg# = 0.24–0.25 and lacks zoning. Plagioclase in GP7f has minor zoning, with a higher-Ca core (An_{22}) that is surrounded by a volumetrically dominant low-Ca (An_{19}) moat, which in turn is surrounded by thin high-Ca rims with An_{20} (Fig. 8B). Plagioclase variations in GP7c show a similar trend to GP7f, with slightly higher-Ca cores (An_{09}) and slightly lower-Ca rims (An_{08}).

AA09-61

Garnet in the mafic dike preserves little chemical variation (Fig. 8C). Grossular content varies from 0.27 to 0.29, with the highest X_{Grs} in the core. The Mg# is 0.11–0.12, with the exception of the rim, where it drops to 0.08. Spessartine content also increases at the rim of the

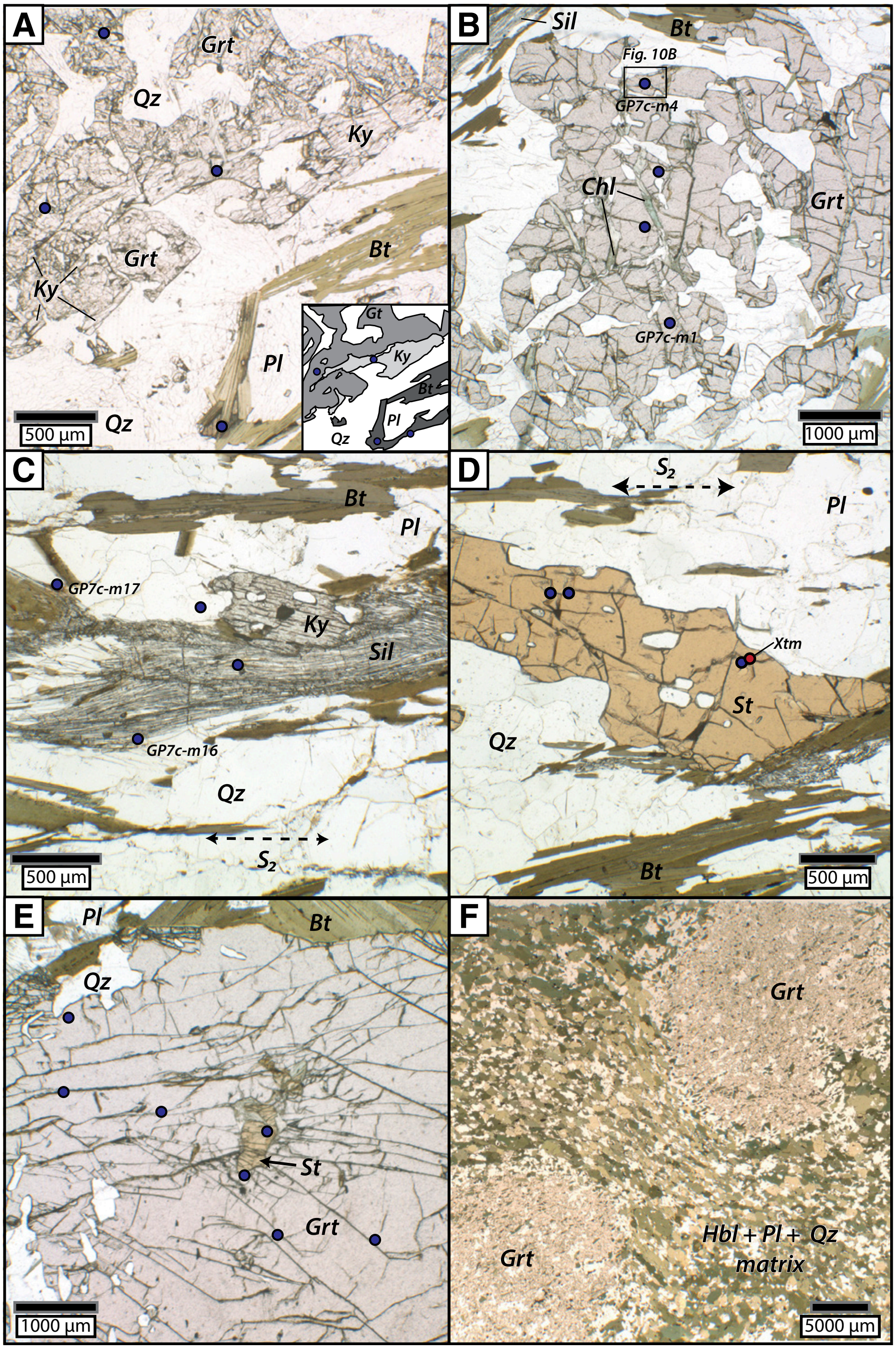

Figure 7. Plane-polarized photomicrographs of key phase relationships in geochronology samples. Blue dots in A–E are locations of monazite, with dated monazite grains labeled. Red dots are xenotime grain locations. (A) Garnet porphyroblast with kyanite inclusion from Bear Basin schist sample GP7c. (B) Garnet porphyroblast containing inclusions of monazite (7c-m4 and 7c-m1 dated) and late fracture-filling chlorite from Bear Basin schist sample GP7c. (C) Fabric (S_2) defining biotite and matrix sillimanite wrapping around kyanite in Bear Basin schist sample GP7c. (D) Staurolite grain containing both monazite and xenotime inclusions in Bear Basin schist sample GP7c. (E) Staurolite included in garnet within Bear Basin schist sample. (F) Photomicrograph of deformed mafic dike sample AA09-61 showing garnet porphyroblasts and Hbl + Pl + Qz matrix. All mineral abbreviations are after Whitney and Evans (2010).

garnet, with an average X_{Sps} of 0.07, rising to 0.11 within 10 µm of the grain edge.

Matrix hornblende and plagioclase have little zoning and are chemically homogeneous across much of the sample. The Mg# values of hornblende inclusions in garnet and in the matrix are 0.33–0.34 and 0.34–0.36, respectively. Hornblende grains in the haloes around garnet have similar compositions. Plagioclase compositions show minimal variation from An_{32} to An_{34}, with plagioclase inclusions in garnet having the higher Ca content. The outer hornblende halo is interpreted to be a prograde feature developed by consumption of plagioclase during synkinematic garnet growth with respect to S_2 development. The inner plagioclase halo is interpreted to have formed during retrogression and partial garnet resorption, which is also supported by the distinct increases in Mn content at the extreme margins of the garnet porphyroblasts.

Thermobarometry and Petrologic Modeling

Thermobarometric calculations and phase assemblage modeling (pseudosection) were used to evaluate equilibrium peak *P-T* conditions and the relative timing of growth of the major metamorphic phases. X-ray maps of targeted garnet and matrix areas were made to evaluate mineral zoning and to ensure that mineral compositions most closely representing peak equilibrium conditions were chosen for *P-T* calculations (e.g., Fig. 8). First, calculations were made using the program TWQ 2.34 (Berman, 1991, http://gsc.nrcan.gc.ca/sw/twq_e.php) and the internally consistent database of Berman and Aranovich (1996; updated in 2007; Berman et al., 2007). Only well-calibrated reactions were used involving garnet, biotite, sillimanite, plagioclase, and quartz for the schist and garnet, and plagioclase, quartz, and hornblende for the mafic dike. Estimated uncertainties associated with these calculations are ±0.1 GPa and ±50 °C (Berman, 1991). All Fe was assumed to be Fe^{2+}. This assumption likely has the greatest effect on the garnet-biotite temperatures, where the results may be overestimated by a few tens of degrees Celsius (Schumacher, 1991). Equilibrium *P-T* conditions for the three samples analyzed were 0.90 GPa, 730 °C for GP7c (Fig. 9A); 0.87 GPa, 700 °C for GP7f (Fig. 9A); and 0.92 GPa, 700 °C for AA09-61 (Fig. 9B). For the Bear Basin schist samples (GP7c and GP7f), duplicate TWQ 2.34 calculations where Fe^{3+} was considered via charge balance for biotite and garnet yielded temperatures ~30 °C lower. Temperature estimates from AA09-61 showed no difference when considering Fe^{3+}. Results from all three samples (~0.9 GPa, 700–730 °C)

TABLE 2. SILICATE COMPOSITIONS

Sample:	GP7c*				GP7f*			AA09-61†								
Mineral:	Grt§	Bt§	Pl§	St§	Grt§	Bt§	Pl§	Grt rim	Grt core	Grt§	Pl rim	Pl (incl. in Grt)	Pl (matrix)§	Hbl (rim)	Hbl (incl. in Grt)	Hbl (matrix)§
SiO_2	38.18	37.42	65.91	27.68	37.91	36.19	62.57	37.40	36.87	36.97	59.46	59.35	60.37	40.47	40.07	40.81
TiO_2	b.d.l.	1.86	–	0.51	b.d.l.	1.50	–	0.01	0.17	0.13	b.d.l.	–	–	1.16	1.13	1.24
Al_2O_3	21.48	17.97	21.85	53.11	20.70	18.70	23.56	21.11	20.66	20.49	25.49	25.71	25.40	13.33	13.11	12.87
FeO	29.39	15.81	0.04	14.18	33.11	17.75	0.03	26.86	25.71	26.12	0.12	0.20	0.14	21.88	22.45	22.34
MnO	4.05	0.10	–	0.41	0.72	0.03	b.d.l.	3.23	3.67	3.57	0.01	0.03	0.02	0.27	0.29	0.29
MgO	7.15	13.69	–	2.65	5.67	11.53	b.d.l.	2.08	1.89	1.94	b.d.l.	b.d.l.	b.d.l.	6.14	6.29	6.65
CaO	0.49	0.01	1.79	b.d.l.	1.34	0.03	3.85	10.00	10.25	9.97	6088	7.02	6.47	11.17	11.05	11.18
Na_2O	–	0.31	10.68	b.d.l.	0.01	0.25	9.25	b.d.l.	0.06	b.d.l.	7.69	7.67	8.01	1.64	1.79	1.84
K_2O	–	9.84	0.09	b.d.l.	–	9.24	0.07	–	–	–	0.10	0.05	0.09	0.94	0.91	0.86
ZnO	–	0.01	–	0.57	–			–	–	–	–	–	–	–	–	–
Total	100.74	97.02	100.36	99.15	99.40	95.04	99.24	100.71	99.27	99.19	99.76	100.03	100.50	97.00	97.09	98.08
End members:	X_{Sps} 0.09	Mg# 0.61	Ab 0.92	Mg# 0.25	X_{Sps} 0.02	Mg# 0.54	Ab 0.77	X_{Sps} 0.07	X_{Sps} 0.08	X_{Sps} 0.08	Ab 0.66	Ab 0.66	Ab 0.69	Mg# 0.33	Mg# 0.33	Mg# 0.36
	X_{Alm} 0.63		An 0.08		X_{Alm} 0.71		An 0.19	X_{Alm} 0.57	X_{Alm} 0.56	X_{Alm} 0.56	An 0.33	An 0.33	An 0.31			
	X_{Prp} 0.27		Or 0.00		X_{Prp} 0.23		Or 0.00	X_{Prp} 0.08	X_{Prp} 0.07	X_{Prp} 0.08	Or 0.01	Or 0.00	Or 0.01			
	X_{Grs} 0.01				X_{Grs} 0.05			X_{Grs} 0.27	X_{Grs} 0.29	X_{Grs} 0.28						
	Mg# 0.30				Mg# 0.24			Mg# 0.12	Mg# 0.12	Mg# 0.12						

Note: Mg#—O-normalized Mg/(Fe + Mg); b.d.l.—below detection limit. Dash indicates element was not measured. Mineral abbreviations from Whitney and Evans, 2010.
*UTM Z12 0470753E, 5021131N.
†UTM Z12 0470816E, 5022885N.
§Composition used in TWQ2.34.

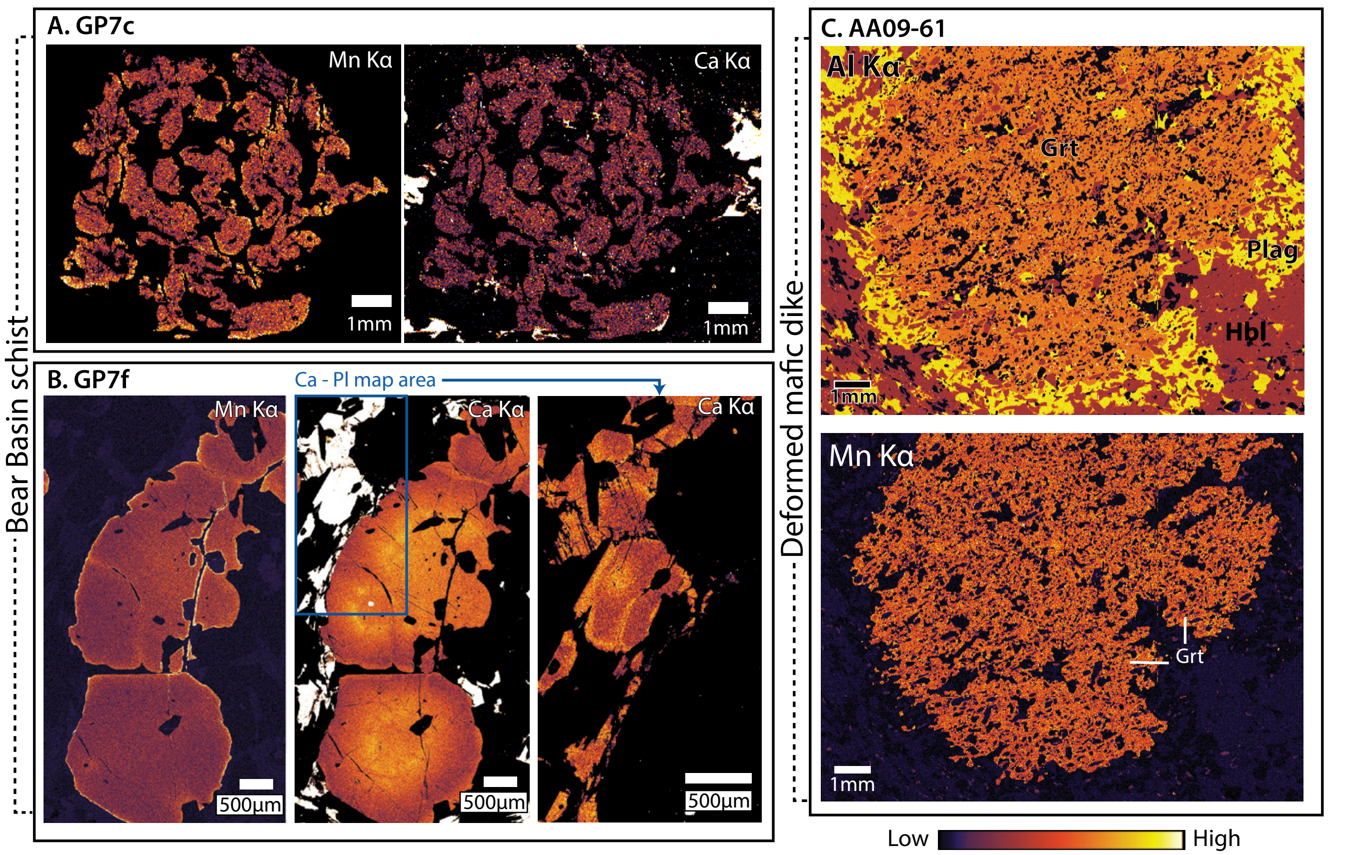

Figure 8. X-ray compositional maps of Bear Basin schist samples GP7c and GP7f and deformed mafic dike AA09-61. Warmer colors indicate higher intensities. (A) GP7c: Mn Kα map adjusted for garnet and Ca Kα map adjusted for garnet. (B) GP7f: Mn Kα map adjusted for garnet, Ca Kα map adjusted for garnet, and Ca Kα map adjusted for plagioclase. (C) AA09-61: Al Kα map, Mn Kα map adjusted for garnet. All mineral abbreviations are after Whitney and Evans (2010).

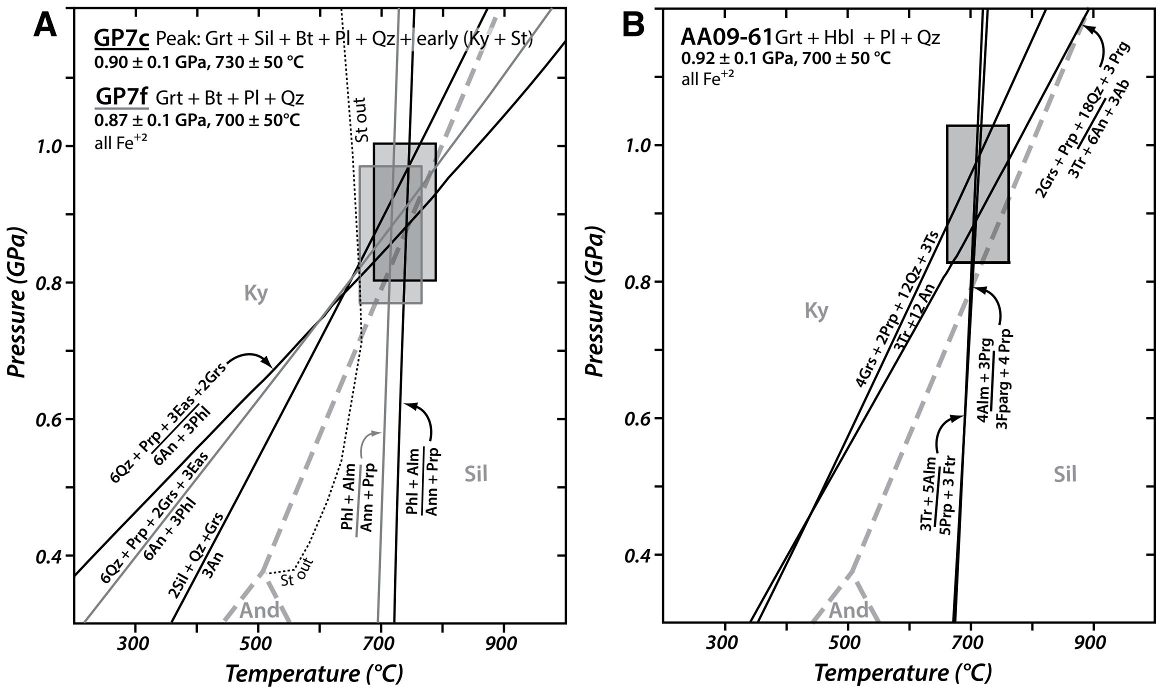

Figure 9. Pressure-temperature diagrams for Bear Basin schist and mafic dike samples AA09-61. (A) Bear Basin Schist sample GP7c in black and sample GP7f in gray. St-out reaction line is shown from phase assemblage models of GP7c in black dotted line. (B) Mafic dike sample AA09-61. All mineral abbreviations are after Whitney and Evans (2010).

are indistinguishable from one another within the estimated range of uncertainty, but the lower end of this temperature range is probably more accurate due to the possible presence of ferric iron in biotite.

Phase assemblage modeling of Bear Basin schist was performed to better understand the relative timing of growth of major mineral phases, the peak equilibrium metamorphic conditions, and to specifically evaluate the likelihood of metastable phases (e.g., staurolite) at higher *P-T* conditions. Modeling of sample GP7c (bulk composition: SiO_2 71.32%, Al_2O_3 14.48%, CaO 0.70%, FeO 4.44%, MgO 2.71%, K_2O 1.69%) in the CaKFMASH system was conducted using PerpleX 6.6.6 (Connolly and Petrini, 2002) with the updated thermodynamic database of Holland and Powell (2011). The results of this modeling indicate maximum thermal stability of staurolite in the range of 670–660 °C over pressures between 0.9 and 0.7 GPa, and stability for the interpreted peak assemblage at conditions consistent with those found using thermobarometric calculations (Fig. 9A).

Geochronology

High-spatial-resolution geochronological techniques are required to analyze accessory minerals because the zircon and monazite grains are small and/or compositionally zoned, with short dimensions of grains or compositional domains commonly ≤20 µm. Monazite and zircon were identified in thin section by automated scanning electron microscope analysis (QEMSCAN) at the Advanced Mineralogy Research Center at the Colorado School of Mines, Golden, Colorado. QEMSCAN instrument parameters are detailed in Ault et al. (2012).

Monazite Analytical Method

Backscatter electron (BSE) images, acquired using a JEOL 8600 electron microprobe at the University of Colorado–Boulder, provided context and textures of select grains. All subsequent mapping and analyses were conducted at the University of Massachusetts–Amherst. X-ray maps for U Mβ, Th Mα, Y Lα, and Ca Kα, and in some cases for Nd Lα, were generated for each monazite grain of interest using a Cameca SX-50 electron microprobe. These maps documented compositional domains and identified areas of interest for quantitative analysis.

U-Th–total Pb monazite dates were acquired using the modified Cameca SX-100 (Ultrachron). Detailed analytical procedures and standard compositions used, including count times, standards, and a list of spectrometers, followed those presented in Appendix A of Dumond et al. (2008), Williams et al. (2006), and Jercinovic et al. (2008). Background collection and subtraction followed the multipoint background method of Allaz et al. (2011). For each chemically homogeneous domain, a weighted average of 3–8 analyses was calculated and reported with a 2σ uncertainty. The reported uncertainty represents the larger of either that calculated by propagating both analytical uncertainty on trace-element compositions through the age equation plus an estimated 1% uncertainty on background intensities (Williams et al., 2006), or two times the standard error of the mean (Table 3). By comparison with X-ray maps and evaluation of the analytical compositions, points that inadvertently sampled a compositional boundary or fell outside of the targeted domain were not included in the weighted mean calculation. The monazite consistency standard used is the Moacyr Brazilian pegmatite monazite with weighted mean isotope dilution (ID) TIMS dates of 506.4 ± 1.0 Ma (2σ, mean square of weighted deviates [MSWD] = 0.6) for $^{208}Pb/^{232}Th$, 506.7 ± 0.8 Ma (MSWD = 0.83) for $^{207}Pb/^{235}U$, and 515.2 ± 0.6 Ma (MSWD = 0.36) for $^{206}Pb/^{238}U$ (W.J. Davis [Geological Survey of Canada], 2007, personal commun.).

Monazite Size, Compositional Zoning, and Textural Context

Monazite grains within the two Bear Basin schist samples, GP7c and GP7f, range in long-axis dimension from ~20 to 140 µm and have shapes ranging from elongate to equant. Grains

TABLE 3. MONAZITE TRACE-ELEMENT COMPOSITIONS AND CALCULATED DATES

Grain	Date analyzed*	Setting	Domain	Pop.	Trace-element concentrations (ppm)								N(n)†	Date (Ma)	2σ (Ma)
					Y	1σ	Th	1σ	Pb	1σ	U	1σ			
GP7c															
M12	4/7/09	g.b. Bt/Qz	Core2	1a	11,626	1250	31,662	1192	8933	851	5574	1196	8(8)	3256	14
M12	4/7/09	g.b. Bt/Qz	Core1	1a	6312	294	21,278	673	3109	216	84	13	6(6)	2995	145
M4	4/7/09	incl. in Grt	Core	1b	10,560	266	38,580	2002	3881	201	2528	74	4(7)	1750	15
M13	4/7/09	incl. in Bt	Rim	2	23,068	602	35,070	512	7156	193	14,523	512	8(8)	1748	8
M1	4/7/09	incl. in Grt	Whole	2	19,490	164	52,773	1187	8320	73	13,791	304	6(8)	1740	10
M4	4/7/09	incl. in Grt	Rim	2	19,410	1245	49,593	2794	7955	212	13,424	619	8(8)	1740	8
M12	4/7/09	g.b. Bt/Qz	Rim	2	21,099	744	32,393	771	6549	114	13,275	291	8(8)	1746	8
M16	4/7/09	incl. in Sil	Rim	2	18,442	873	49,559	1331	8936	244	17,122	434	8(8)	1723	8
M17	4/7/09	assoc. Sil	Rim	2	20,466	1081	50,574	1776	8782	262	16,263	439	8(8)	1726	8
GP7f															
M3	2/16/12	incl. in Bt	Core	1b	1589	1619	55,258	3311	6153	383	5604	311	3(3)	1752	10
M9	2/6/12	g.b. Bt/Ilm	Core	1b	3158	190	46,087	934	5184	72	5186	83	5(7)	1722	12
M28	2/6/12	incl. in Pl	Core	1b	2991	182	44,978	2091	4940	200	4669	202	5(5)	1721	15
M36	2/6/12	incl. in Grt	Core	1b	4489	108	53,709	1177	5960	18	5595	242	4(6)	1735	18
M6	2/6/12	incl. in Qz	Inner rim	2	670	42	53,974	275	9009	80	15,884	95	5(6)	1736	9
M3	2/6/12	incl. in Bt	Inner rim	2	1265	153	56,617	839	7771	149	10,919	357	4(5)	1738	9
M23	2/6/12	incl. in Pl	Inner rim	2	1206	55	56,383	335	8294	27	13,098	58	5(6)	1720	5
M3	2/6/12	incl. in Bt	High-Y rim	3	12,124	744	45,680	430	4446	35	2910	108	4(4)	1706	10
M6	2/6/12	incl. in Qz	High-Y rim	3	3993	48	55,781	197	7291	36	10,074	123	8(8)	1704	10
M8	2/6/12	incl. in Pl	High-Y rim	3	4439	172	55,075	360	6976	90	9133	160	8(8)	1706	11
Consistency standard															
	2/6/12				11,326	86	62,111	72	1468	17	850	22	5	504	5
	2/6/12				11,235	68	61,607	96	1496	20	885	12	5	507	6
	4/6/09				11,389	60	62,901	272	1478	18	701	24	6	504	5
	4/7/09				11,290	169	63,190	890	1464	10	680	25	3	498	9

Note: g.b.—grain boundary; incl—inclusion. Mineral abbreviations from Whitney and Evans, 2010.
*Dates are month/day/year.
†*N*—number of points used for domain date; *n*—total number acquired.

occur throughout the quartzofeldspathic matrix and are commonly included in, or in close proximity to, all major metamorphic phases (Grt, Ky, St, Sil, and Bt; Figs. 7A–7E). Three distinct monazite domain populations occur in the two samples, based primarily on composition, as well as supporting evidence from grain textures and zoning patterns. Therefore, some grains may contain more than one population. Population 1 consists of low-U core domains (≤0.5 wt% U; Table 3; Figs. 10A–10C). Population 2 consists of domains defining whole grains, inner rims (Fig. 10C), or outer rims with >1 wt% U (Fig. 10B). Both of these populations occur in grains located in the matrix, as inclusions in garnet in both samples, and as inclusions in kyanite and staurolite in sample GP7c. Grains with rim domains of population 2 are also locally intergrown and included within foliation-defining sillimanite in GP7c (Fig. 7C). Monazite with population 3 domains only occurs in the less-aluminous schist sample GP7f, where grains locally exhibit thin (~5–10 μm), relatively high-Y rims (Figs. 10C–10D). These population 3 rim domains all contain 4–10 times the Y content of the core domains within the same grain. Grain GP7f-m3 contains all three populations (Fig. 10C). Both samples contain elongate monazite grains with long axes subparallel to a local S_1 or S_2 fabric (Figs. 10C and 10D). For example, grain GP7f-m3 contains a population 3 domain that forms an asymmetric tip aligned with the S_2 fabric (Fig. 10C).

Monazite Geochronology Results

Thirty-four grains were investigated through BSE and X-ray maps, and quantitative data were collected from 19 domains in 14 grains from the two schist samples (seven grains from each sample; Table 3; Fig. 11). This selection of grains represents the full range of textural settings and morphologies described earlier. Two population 1 domains from monazite GP7c-m12, a matrix grain occurring at the contact between biotite and quartz, yield Mesoarchean dates of 2995 ± 145 Ma and 3255 ± 14 Ma (all errors 2σ; Fig. 10A). All other population 1 domains, which represent the cores of several matrix grains, as well as the cores of two grains included in garnet (one from each sample), yield dates between 1752 ± 10 Ma and 1721 ± 15 Ma. Thus, population 1 was subsequently split into Archean population 1a and Paleoproterozoic population 1b, but no distinguishing characteristics other than age are apparent. Population 2 dates range from 1748 ± 8 Ma to 1720 ± 5 Ma, and they are mostly from rim domains of matrix grains, including two intergrown with sillimanite, but also include one whole grain and one rim domain included in garnet (Table 3). There is no apparent statistical distinction of dates from grains of different orientation (Figs. 10C–10D). The youngest dates are from population 3 rim domains in GP7f, ranging from 1706 ± 11 Ma to 1704 ± 10 Ma.

Zircon Analytical Method

BSE and cathodoluminescence (CL) images of selected zircon targets were used to assess zoning and reveal internal grain structure. BSE images were acquired at the University of Colorado–Boulder, and CL images were taken at the University of Wyoming, Laramie, Wyoming. The thin section was trimmed into ≤7-mm-diameter chips containing the target zircon. The chips were mounted in epoxy, polished, cleaned, and coated with a nanometer-thick conductive coating of Au as detailed in Schmitt et al. (2010). Mounts also contained zircon standard AS3 (1099 ± 1 Ma; Paces and Miller, 1993). The U standard was NIST 91500 (Wiedenbeck et al., 1995).

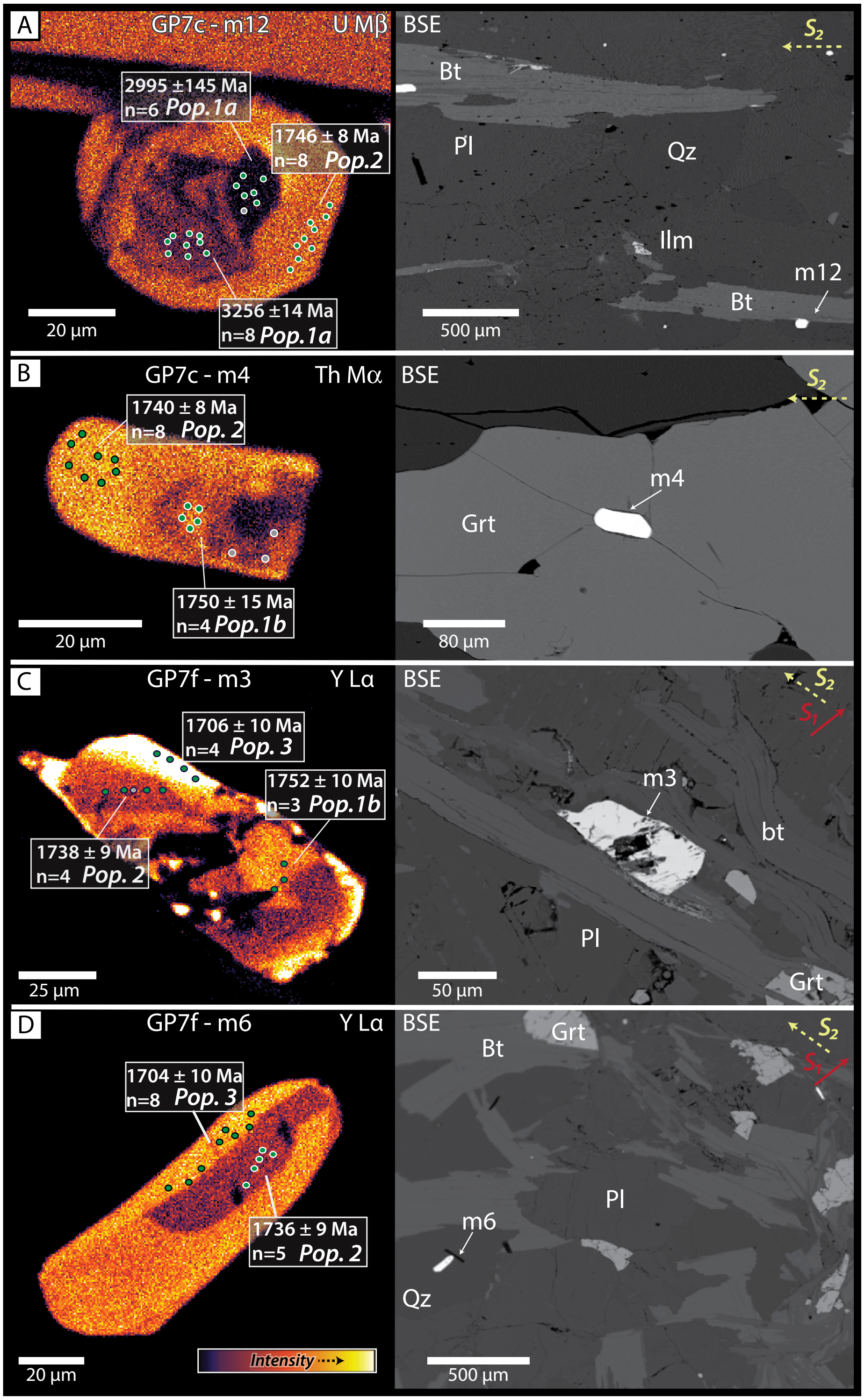

Figure 10. Monazite X-ray intensity maps and backscattered-electron (BSE) textural images for Bear Basin schist. X-ray maps are annotated with electron microprobe (EMP) analysis spots in green (rejected points in gray), population designations, and U-Th–total-Pb EMP domain dates. (A–B) Monazite from GP7c. (C–D) Monazite from GP7f. All mineral abbreviations are after Whitney and Evans (2010).

Quantitative isotopic analyses were done on the high-sensitivity Cameca ims 1270 ion microprobe at the University of California–Los Angeles. The field aperture of the ims 1270 was adjusted to subsample secondary ions emitted from the interior of the primary beam pit in order to analyze grains with minimum dimensions as small as 4 µm at radiogenic yields typically >95% for radiogenic ^{206}Pb (^{206}Pb*). The reduction in the field aperture suppressed common Pb, and the surface was flooded with oxygen gas to increase the Pb* yield. The instrument operating conditions and procedures performed to optimize secondary ion yields for the present study were described in detail by Grove et al. (2003) and Schmitt et al. (2010). Zircon standard AS3 was measured at the beginning and end of each analytical session, during which a two-point linear drift correct was applied to the data. Th was not measured.

Zircon Morphology and Textural Occurrence

Of the 43 zircon grains evaluated in detail (optically and through BSE imaging), two zircon populations were identified in this sample based on morphology and texture. Although CL images were acquired, the internal structure of the grains is more clearly visible in BSE images. Zircon grains from AA09-61 range from 17 to 60 µm along their long axis. Similar to the monazite, zircon population distinctions are specific to domains, of which more than one commonly occur in a single zircon grain. Population 1 domains are distinctly inclusion rich and commonly contain small patchy variations in brightness in BSE images. Some zircons consist entirely of population 1 domains (Fig. 12A), but most contain population 1 domains as cores (Figs. 12B–12D). Population 2 domains are inclusion free and exhibit little to no zoning. They occur as rims of variable thickness around inclusion-rich population 1 domains (e.g., Figs. 12C and 12D) and as whole grains (Figs. 12E–12F). Texturally, zircons with population 1 domains occur as inclusions in garnet, in the hornblende and plagioclase haloes around garnet, and in the matrix. Zircon containing population 2 domains occurs in all of the same settings, but is more common in the matrix.

Zircon Geochronology Results

Twenty-four grains were selected for U-Pb analysis representing the full range of textural settings and grain sizes (Table 4). Of the 24 grains dated, eight grains were associated with garnet porphyroblasts, either as inclusions in garnet, inclusions within phases included in the garnet, or within the plagioclase and hornblende haloes around the porphyroblastic garnet. Sixteen zircon

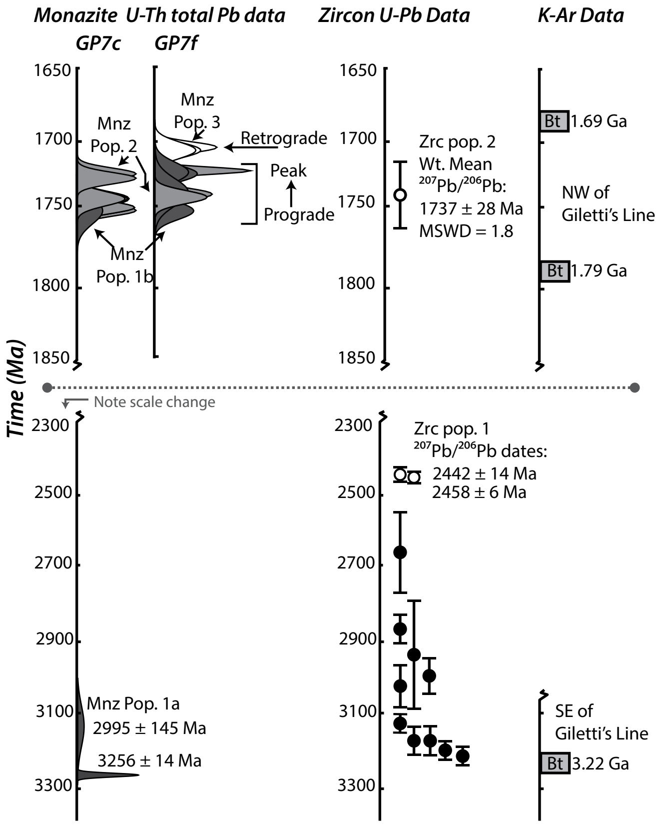

Figure 11. Monazite (this study), zircon (solid black circles are from Weyand, 1989; open circles are this study), and K-Ar (Giletti, 1966) geochronology data from the SE part of the Northern Madison Range. MSWD—mean square of weighted deviates.

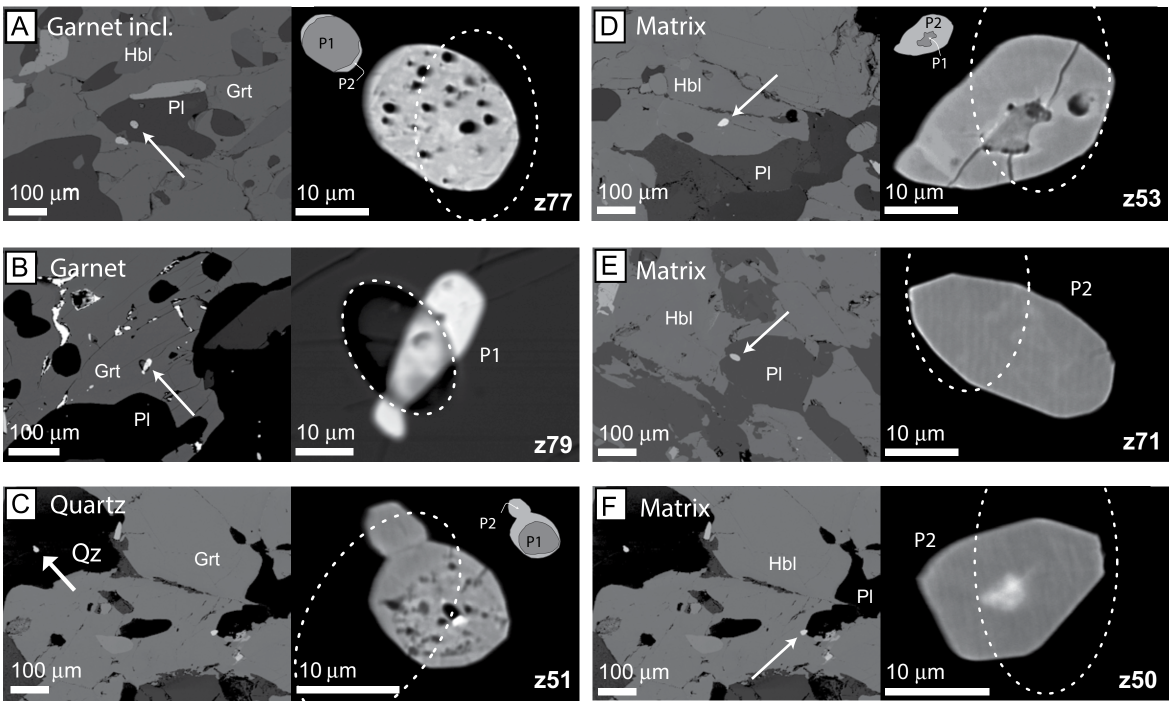

Figure 12. Backscattered-electron (BSE) images from select dated zircon in AA09-61. P1 is population 1 zircon, and P2 is population 2 zircon in annotated images and grain schematics. Dotted white ellipses indicate secondary ion mass spectrometry (SIMS) beam locations on each grain. (A–D) Examples of zircons with inclusion-rich cores of zircon population 1, and varying amounts of inclusion-free rims of zircon population 2. (E–F) Grains lacking inclusion-rich cores, being completely composed of zircon population 2. All mineral abbreviations are after Whitney and Evans (2010).

TABLE 4. SECONDARY ION MASS SPECTROMETRY (SIMS) U-Pb ZIRCON ANALYSES FROM AA09-61

Grain	Textural setting	Pop.	Max. axis* (mm)	Min. axis† (mm)	$^{206}Pb/^{238}U$	±	$^{207}Pb/^{235}U$	±	$^{207}Pb/^{206}Pb$	±	U (ppm)	^{206}Pb§ (%)	Dates (Ma) $^{206}Pb/^{238}U$	±	$^{207}Pb/^{235}U$	±	$^{207}Pb/^{206}Pb$	±
z77	in Pl incl. in Grt	1	21	17	0.4630	0.0207	10.2000	0.4590	0.1600	0.0003	3445	99.98	2453	91.4	2456	41.5	2458	2.75
z79	in Grt	1	30	11	0.4340	0.0182	9.4900	0.4040	0.1590	0.0007	517	99.67	2323	82	2387	39.1	2442	7.06
z51	in Qz	Mixed	17	11	0.3563	0.0109	7.4260	0.2290	0.1512	0.0003	3024	99.95	1965	51.7	2164	27.6	2359	3.38
z41	in Grt	Mixed	18	14	0.3360	0.0112	6.7300	0.2250	0.1450	0.0003	1784	99.87	1867	54.2	2077	29.6	2291	3.7
z92	matrix g.b.	Mixed	61	28	0.3270	0.0153	7.1700	0.3380	0.1590	0.0003	5093	99.91	1823	74.5	2133	42	2447	3.6
z23	in Grt	Mixed	18	12	0.2070	0.0108	3.6300	0.2030	0.1270	0.0022	233	97.41	1214	57.9	1557	44.5	2058	30.6
z59	in Hbl halo	Mixed	42	19	0.1720	0.0092	3.1000	0.1660	0.1310	0.0005	4503	99.22	1023	50.7	1432	41.2	2107	6.25
z53	in Hbl	Mixed	31	17	0.1402	0.0053	2.7270	0.2700	0.1410	0.0114	484	84.93	846	29.9	1336	73.6	2240	139
z78	in Pl-Grt g.b.	Mixed	27	17	0.1200	0.0050	1.9700	0.0828	0.1190	0.0010	2409	99.00	731.4	28.6	1105	28.3	1940	14.5
z30	matrix g.b.	Mixed	27	18	0.1148	0.0063	1.9160	0.1290	0.1211	0.0042	448	91.99	700.3	36.4	1087	44.8	1972	61.1
z109	matrix g.b.	2	48	15	0.4159	0.0244	5.9250	0.3640	0.1033	0.0016	67	98.31	2242	111	1965	53.4	1685	29.1
z145	in Grt	2	20	16	0.4070	0.0321	6.0900	0.5490	0.1090	0.0036	73	98.01	2202	147	1989	78.6	1774	61.2
z48	matrix g.b.	2	36	12	0.3800	0.0192	5.4760	0.3320	0.1045	0.0035	46	97.02	2076	89.5	1897	52	1706	61.6
z34	matrix g.b.	2	34	18	0.3844	0.0341	5.7940	0.5220	0.1093	0.0025	28	99.75	2097	159	1946	78	1788	41.9
z63	matrix g.b.	2	27	19	0.3451	0.0215	4.8190	0.3730	0.1013	0.0037	32	96.82	1911	103	1788	65.1	1648	68
z144	in Pl rim	2	17	10	0.2770	0.0145	4.4600	0.3200	0.1170	0.0050	46	94.86	1577	73.4	1724	59.5	1906	77
z85	matrix g.b.	2	25	16	0.3607	0.0182	5.2870	0.2720	0.1063	0.0013	58	99.4	1985	86.3	1867	43.9	1737	22.9
z91	matrix g.b.	2	23	21	0.3370	0.0246	4.8600	0.3670	0.1050	0.0020	34	99.43	1872	119	1795	63.6	**1706**	35.4
z69	matrix g.b.	2	36	16	0.3258	0.0124	4.6580	0.1960	0.1037	0.0015	73	99.00	1818	60.5	1760	35.1	**1692**	25.8
z71	matrix g.b.	2	28	14	0.3341	0.0176	4.9340	0.2750	0.1071	0.0023	44	99.32	1858	85	1808	47	**1750**	38.7
z31	matrix g.b.	2	30	24	0.3345	0.0200	4.9500	0.3060	0.1073	0.0017	56	99.17	1860	96.6	1811	52.2	**1755**	28.5
z50	matrix g.b.	2	17	12	0.3538	0.0194	5.5750	0.3680	0.1143	0.0037	58	96.17	1953	92.2	1912	56.9	**1869**	59
z52	in Hbl	2	25	13	0.3175	0.0167	4.8230	0.2990	0.1102	0.0033	58	96.43	1778	81.7	1789	52.1	**1802**	54.8
z112	matrix g.b.	2	32	14	0.2850	0.0177	4.2100	0.3280	0.1070	0.0044	44	96.41	1615	89	1676	64	**1753**	75.2

Note: **Bold** $^{207}Pb/^{206}Pb$ dates used for population 2 weighted mean of 1737 ± 28 Ma (2σ, mean square of weighted deviates [MSWD] = 1.8); g.b.—grain boundary. Mineral abbreviations from Whitney and Evans, 2010.

*Maximum axis dimension.

†Minimum axis dimension.

§Uncertainties give at 1σ.

grains were analyzed from the matrix. Two of these 16 grains were within matrix hornblende, one was within matrix quartz, and the remaining one was are located along grain boundaries.

The U contents from the analyses provide additional distinction between populations 1 and 2. Zircon composed of dominantly population 1 had >500 ppm U, whereas analyses of whole grains of population 2 were <100 ppm U (Table 4). Analyses with U concentrations between 100 and 500 ppm U were those from grains with significant fractions of cores and rims where the beam likely sampled both domains (e.g., Figs. 12C–12D).

Two zircon analyses that sampled predominantly population 1 domains (z77, z79; Figs. 12A–12B) yielded concordant analyses (at 1σ) at ca. 2.45 Ga ($^{207}Pb/^{206}Pb$ dates of 2458 ± 3 Ma and 2442 ± 7 Ma; Fig. 13A), with U concentrations in excess of 500 ppm (Table 3; Fig. 13B). Grain z79 is in garnet (Fig. 12B), and z77 is completely included in plagioclase, which is itself an inclusion in garnet (Figs. 12A and 13C). Analyses that sampled both cores and rims in multidomain grains were discordant (Figs. 12C–12D), with $^{207}Pb/^{206}Pb$ dates ranging between 1940 Ma ± 15 Ma (z41) and 2447 ± 4 Ma (z91). These analyses also had U concentrations >100 ppm. The array of discordant analyses likely reflects mixing as a result of sampling two age domains coupled with recent Pb loss. The recent Pb loss had a more noticeable effect on analyses sampling mixed domains of predominantly population 1, with the higher U concentrations (Table 4; Fig. 13B). Analyses of exclusively population 2 zircon were either concordant or reversely discordant, and together yielded a $^{207}Pb/^{206}Pb$ date of 1732 ± 21 Ma (2σ, MSWD = 1.5, n = 12). The seven analyses that overlapped concordia at 1σ have a weighted mean $^{207}Pb/^{206}Pb$ date of 1737 ± 28 Ma (2σ, MSWD = 1.8; Table 3; z71 and z50 are examples; Figs. 12E, 12F, and 13, inset). This date is our preferred timing of population 2 zircon growth.

DISCUSSION

Nature and Timing of Tectonometamorphism in the Northwest Gallatin Peak Terrane

At least three phases of deformation affected the northwest Gallatin Peak terrane. D_1 structures are likely composite, and zircon U-Pb data from the mafic dike point to an Archean age for at least some component of this deformation. Population 1 zircon is unlikely to be inherited because it would require the dike magma to have sampled an as-yet-unrecognized 2.45 Ga source while avoiding the widely recognized 3.2–3.0 Ga sources in the region. Thus, based on the most concordant data from population 1 zircon, the minimum age of the mafic dike that obliquely crosscuts S_1 fabric in the host tonalitic gneiss (Figs. 4C–4D) is ca. 2.45 Ga. Whether this population of zircon is magmatic or metamorphic is not yet clear. Support for the latter comes from a ca. 2.45 Ga metamorphic event recognized in the Tobacco Root Mountains and elsewhere in southwest Montana (Roberts et al., 2002; Cheney et al., 2004; Foster et al., 2006; Loehn, 2009; Krogh et al., 2011) and Utah (Mueller et al., 2011). The 2.45 Ga age may be synchronous with the deformation event that produced the foliation locally recorded as inclusion trails in garnet from this dike (also listed in the broad category of D_1 structures here). These data also imply that at least this dike in the Gallatin Peak terrane cannot be part of the suite from which a 2.06 Ga mafic dike was dated in the Tobacco Root Mountains (Mueller et al., 2004, 2005; Brady et al., 2004b).

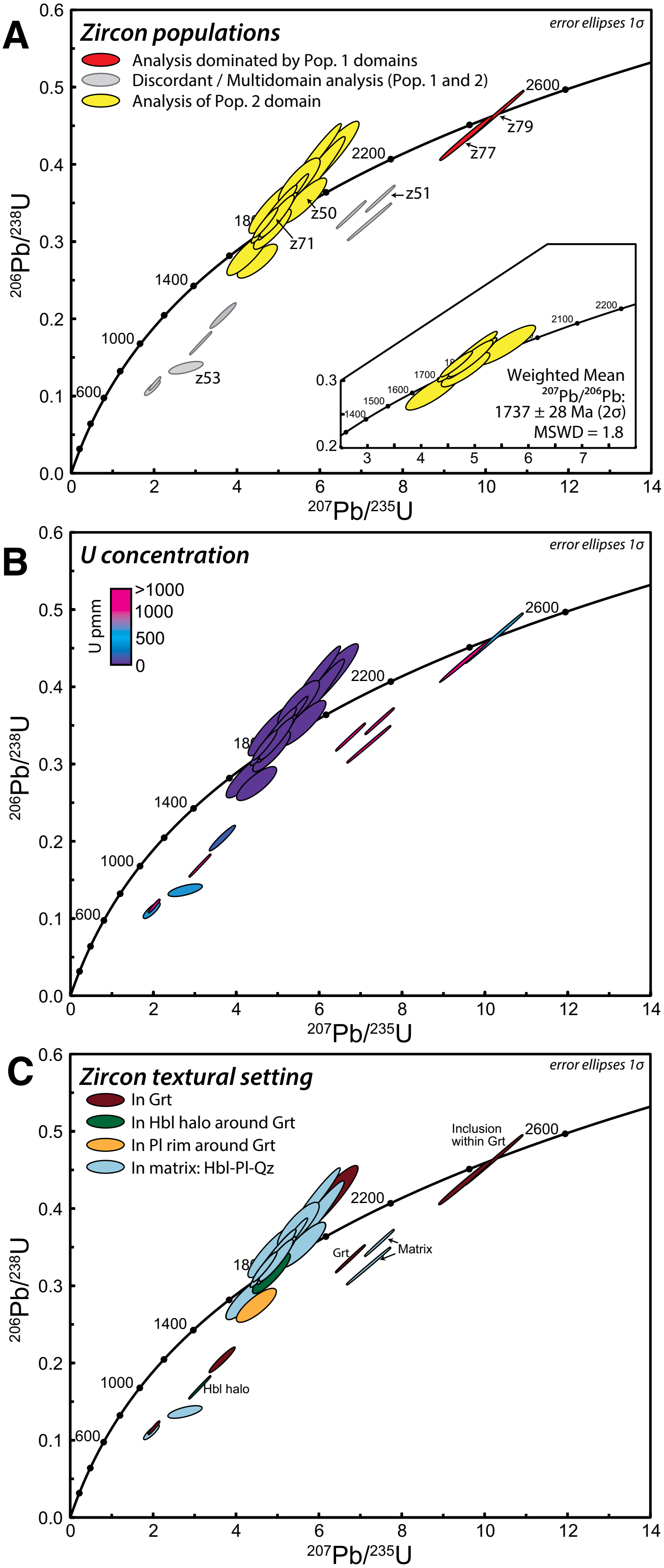

Figure 13. U-Pb concordia diagrams for AA09-61 zircon analyses. (A) Ellipse classified by domain. Population 1 domains yield two concordant grains at ca. 2.45 Ga. Mixed analyses of both population 1 and 2 domains are mostly discordant due to mixing and Pb loss. Population 2 domains are all concordant or slightly reversely discordant. All analyses of population 2 domains that overlap concordia yield a Paleoproterozoic ^{207}Pb/^{206}Pb weighted mean date (inset). (B) Ellipses classified by U content (ppm). (C) Ellipses classified by zircon textural setting. MSWD—mean square of weighted deviates. All mineral abbreviations are after Whitney and Evans (2010).

D_2 structures are the most prominent deformation features in the terrane and studied samples. The prograde and peak mineral phases in the Bear Basin schist (e.g., Ky, St, Sil, Bt) and in the mafic dike (e.g., Hbl) are aligned with this fabric (including Ky locally defining L_2 mineral lineation), suggesting that peak metamorphism was synkinematic with respect to D_2.

Local kyanite and staurolite inclusions in garnet contrast with sillimanite occurrence solely in the matrix, suggesting that sillimanite stability followed that of kyanite and staurolite on a portion of a clockwise *P-T* path recorded by the Bear Basin schist. Thermobarometry from peak synkinematic assemblages in all samples yielded *P-T* conditions of ~0.9 GPa and ~700 °C. These conditions are near the Ky-Sil reaction line (Fig. 9), which is consistent with the presence of both aluminosilicates in the schist. Peak temperatures exceeded those predicted for staurolite stability from phase assemblage modeling. This is consistent with staurolite solely occurring as inclusions in garnet in some samples (Fig. 7C). These results are similar to undated conditions reported by Salt (1987) and Mogk et al. (1992) for the Gallatin Peak terrane. Clockwise *P-T* paths are inferred for other exhumed crystalline rocks in the Tobacco Root Mountains (Cheney et al., 2004) and the Ruby Range (Alcock et al., 2013).

The new data presented here indicate that D_2 deformation and prograde and peak metamorphism occurred in the northwest Gallatin Peak terrane ca. 1750–1720 Ma. This is supported both by zircon U-Pb data from the deformed mafic dike and by monazite U-Th–total Pb data from the Bear Basin schist. The morphology and lack of zoning in population 2 zircon domains are typical of metamorphic zircon (Corfu et al., 2003). These grains, with a weighted mean ^{207}Pb/^{206}Pb date of 1737 ± 28 Ma, occur as inclusions in garnet as well as in the matrix associated with S_2-aligned hornblende or plagioclase. Thus, garnet in the mafic dikes grew near or after ca. 1740 Ma. These observations also indicate that the S_2 fabric, which wraps around the garnet porphyroblasts, developed during or after garnet growth.

U-Pb analyses of zircon with population 1 and 2 domains are in some cases discordant, in part because the ion probe primary beam likely sampled both domains (Figs. 12C–12D). Results thus reflect both mixing between ca. 2.45 Ga cores and ca. 1.74 Ga rims and recent Pb loss. Grains with higher U are more susceptible to radiation damage-enhanced Pb loss, impacting the degree of discordance of these analyses (Fig. 13B).

Monazite populations 1b and 2 (1750–1720 Ma) are interpreted to have grown during prograde and peak metamorphism because they occur as inclusions in all major metamorphic phases (garnet, kyanite, staurolite) and in the matrix of the Bear Basin schist. In general, monazite in low-Ca pelitic bulk compositions, such as the Bear Basin schist, is commonly thought to become stable around the staurolite-in isograd (Kohn and Malloy, 2004) and to continue growing throughout the duration of a metamorphic event (Spear and Pyle, 2010).

An interpretation of episodic synmetamorphic monazite growth is further supported by distinct compositional variations between the populations. For example, Y content increases by a factor of two between populations 1b and 2 in sample GP7c, whereas the opposite trend is recorded in sample GP7f. However, both trends can be explained by prograde metamorphic growth, considering that monazite Y compositions are commonly dependent on the behavior of other Y-bearing phases such as xenotime and garnet (e.g., Spear and Pyle, 2010). In xenotime-bearing lithologies, monazite Y concentrations generally increase with increasing metamorphic grade (Pyle et al., 2001), tracking the progressive destabilization of xenotime. Observed xenotime inclusions in staurolite and total Y contents in monazite that are approximately an order of magnitude higher in GP7c than GP7f indicate that xenotime was a stable phase for a portion of the prograde sequence in GP7c. In contrast, xenotime was probably never stable in GP7f, and the decreasing trend in Y content in monazite between GP7f populations 1b and 2 probably reflects progressive depletion in available bulk Y as both garnet and monazite continued to grow. Thus, the range in population 1b and 2 monazite dates is interpreted to represent episodic growth through the main duration of late Paleoproterozoic metamorphism. Cheney et al. (2004) came to a similar conclusion for monazite data from an ion probe study of rocks in the Tobacco Root range.

Monazite population 3 has the highest Y content and dates that cluster around ca. 1705 Ma. The increase in Y is interpreted to reflect retrograde breakdown of garnet, which liberates Y into the system (Pyle et al., 2001; Gibson et al., 2004; Mahan et al., 2006). This is supported by evidence of late garnet resorption (Figs. 8A–8B), which may be due to fluid flow and/or exhumation after peak thermotectonism. Finally, the one Archean monazite grain identified in the Bear Basin schist (population 1a) could be either metamorphic or detrital. Weyand (1989) dated 3.1 Ga detrital zircon in schist from this unit, and a detrital origin for this similarly aged monazite is consistent with its textural location in a quartzofeldspathic layer (Bt + Pl + Qz only). Possible detrital sources are nearby, since the unit appears to sit in depositional contact with 3.2–3.1 Ga orthogneiss.

Patterns of Exhumation and Timing of the Big Sky Orogeny in Southwest Montana

Paleodepths across the Northern Madison Range

Our new results, combined with previously published data, suggest that exhumed tracts of rocks characterized by broadly decreasing Proterozoic paleodepth are exposed across the Northern Madison Range, and may extend farther to the southeast (Figs. 1 and 2). Of reported thermobarometric conditions across the range, two have timing constraints and are known to represent ca. 1.7 Ga paleodepths. These are ~45–40 km near the Madison River (1.2 GPa metamorphic pressure in Bear Trap Canyon; Ault et al., 2012), which may be the deepest in southwest Montana, and ~30 km in Bear Basin (~0.9 GPa; this study). Thus, as much as a 15 km difference in paleodepth is recorded over a map distance of 30 km across strike of the dominant structural grain (Fig. 2).

K-Ar mica data were used to demarcate the transition in southwest Montana from complete to negligible Paleoproterozoic thermal resetting toward the interior of the Wyoming craton (Giletti, 1966). The original location of this boundary (Giletti's line) passes through Gallatin Canyon, ~15 km across strike and southeast from Bear Basin (Figs. 1 and 2). This would appear to require a rapid shallowing to the southeast of Proterozoic paleodepths to upper-crustal levels (i.e., ~10 km) over 15 km from our farthest east paleodepth constraint of ~30 km. However, problems with excess Ar brought into question the validity of the key Gallatin Canyon data (Giletti, 1971), and the true location of this thermal boundary in the Northern Madison range is still uncertain.

A tilted partial crustal section, stacked thrust sheets, or stacked fold nappes are among several viable options that could currently explain the constrained differences in paleodepth. Several previously identified but as yet poorly understood high-strain zones within the range, including the Hellroaring Creek shear zone (Fig. 2), may represent bounding structures of thrust sheets or nappes. More detailed work in the region is clearly justified given the general utility of partial crustal sections for better understanding the growth and evolution of orogenic crust (Percival et al., 1992; Miller and Snoke, 2009). Farther to the south, faulting at greenschist facies in the Southern Madison Range (Fig. 1; Madison Mylonite zone of Erslev and Sutter, 1990) and along-strike localities to the northeast (Mogk and Henry, 1988; Erslev, 1989) may represent upper-crustal deformation in the foreland region of the Big Sky orogeny (O'Neill, 1998; Harms et al., 2004a).

Propagation of Proterozoic Tectonometamorphism across Southwest Montana

The spatial extent of the Big Sky orogen is poorly constrained, partly because it is only exposed in younger, isolated basement-cored uplifts (Fig. 1A). Previous studies invoke a ca. 1.80–1.71 Ga time interval for the Big Sky orogeny (e.g., Harms et al., 2004a). Some have suggested that it may represent the closure of a late Paleoproterozoic ocean basin (O'Neill, 1998; Roberts et al., 2002; Harms et al., 2004a; Vogl et al., 2004; Mueller et al., 2005; Foster et al., 2006; Alcock et al., 2013), recorded by ca. 1.86 −1.81 Ga arc-related granitoid rocks in the Little Belt Mountains (Fig. 1A; Mueller et al., 2002; Vogl et al., 2004).

New data presented here, along with previously published monazite and zircon geochronology, suggest a southeastward younging of high-grade metamorphism in SW Montana. The details of this observation provide important constraints on the pace, duration, and spatial patterns of hinterland growth in the Big Sky orogen. Figure 14A shows a compilation of all published zircon, monazite, and garnet geochronological data younger than 1900 Ma that we are aware of, plotted along a 150 km SE-trending profile centered among the basement exposures of SW Montana. The orientation of this profile was chosen to cross the structural grain of the dominant strike of major structures (e.g., foliation planes, fold axes, shear zones), the overall trend of Giletti's line, and the Great Falls tectonic zone. This figure focuses on data that are linked to timing of peak metamorphic conditions equal to or exceeding 700 °C, although igneous zircon U-Pb data and ^{40}Ar-^{39}Ar data for mica and amphibole are also plotted for additional context. The southeastward younging trend of high-grade metamorphism is separately apparent from both monazite and zircon data

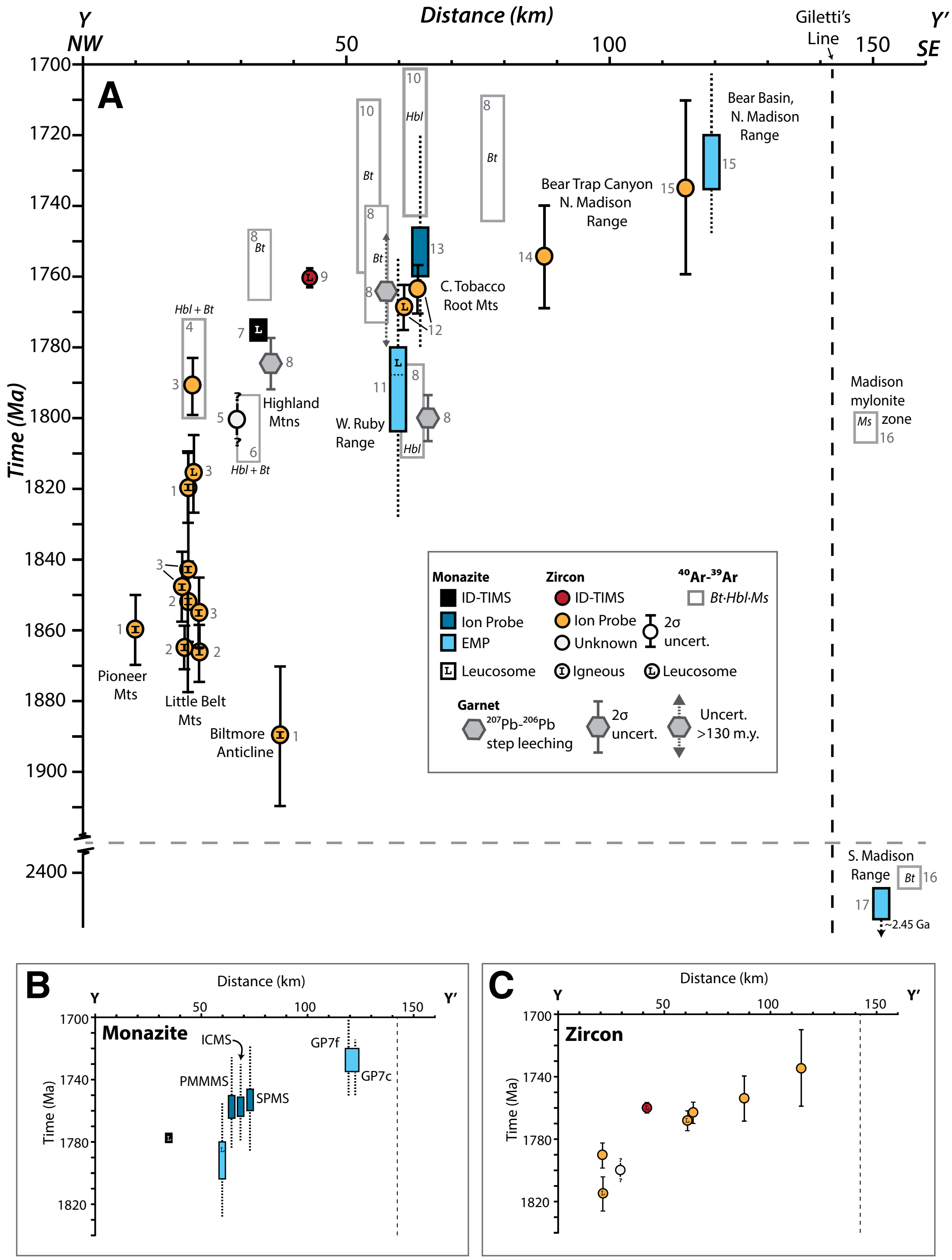

Figure 14. (A) Time-space plot of U-Pb zircon, monazite, and garnet geochronology data interpreted to represent mineral growth during peak metamorphism (≥700 °C) across southwest Montana projected onto cross-section line Y–Y′ found on Figure 1A. Also plotted are ^{40}Ar/^{39}Ar thermochronology data and igneous zircon crystallization data. Range of data for monazite is shown with dotted black lines, with interpreted timing of peak metamorphism designated by colored boxes. Data sources are: 1—Foster et al. (2006), 2—Mueller et al. (2002), 3—Vogl et al. (2004), 4—Holm and Schneider (2002), 5—O'Neill et al. (1988), 6—Harlan et al. (1996), 7—Mueller et al. (2005), 8—Roberts et al. (2002), 9—Krogh et al. (2011), 10—Brady et al. (2004a), 11—Alcock et al. (2013), 12—Mueller et al. (2004), 13—Cheney et al. (2004a), 14—Ault et al. (2012), 15—this study, 16—Erslev and Sutter (1990), 17—Loehn (2009). ID-TIMS—isotope dilution–thermal ionization mass spectrometry; EMP—electron microprobe. All mineral abbreviations are after Whitney and Evans (2010). (B) Time-space plot of metamorphic monazite geochronology data. PMMMS—Pony–Middle Mountain metamorphic suite, ICMS—Indian Creek metamorphic suite, SPMS—Spuhler Peak metamorphic suite from Tobacco Root Mountains (Cheney et al., 2004b). Sources same as in A. (C) Time-space plot of metamorphic or leucosomal zircon geochronology data. Sources same as in A.

sets and from isotopic (ion probe) and nonisotopic (U-Th–total Pb) techniques (Figs. 14B and 14C), suggesting no systematic bias from different mineral systems or analytical approaches. Additional description of the plotted data is given in the following paragraphs.

Within the Great Falls tectonic zone, there is evidence of late Paleoproterozoic arc magmatism in the Little Belt Mountains (Fig. 1A), Pioneer Mountains, and Biltmore anticline (Fig. 14A; Mueller et al., 2002; Vogl et al., 2004; Foster et al., 2006). Igneous zircon crystallization ages range from ca. 1890 to 1810 Ma (Vogl et al., 2004; Foster et al., 2006), while subsequent metamorphism and anatexis may have occurred in the Little Belt Mountains at ca. 1820–1790 Ma (Vogl et al., 2004).

In the most northwestern exposures of non-arc-related Precambrian rocks in the Highland Mountains (Fig. 1B), previous U-Pb zircon and monazite and Pb-Pb garnet studies concluded that peak metamorphism occurred ca. 1800–1770 Ma (O'Neill et al., 1988; Roberts et al., 2002; Mueller et al., 2005). Farther southeast across strike (~40 km) in the Ruby Range, Pb-Pb garnet dates were similarly interpreted to record garnet growth and metamorphism from ca. 1800 to 1780 Ma (Roberts et al., 2002). This history is also supported by a more recent monazite U-Th–total Pb study of migmatitic metapelites (Alcock et al., 2013). These authors interpreted prograde metamorphism as early as ca. 1830 Ma, but culminating at ca. 1780 Ma. In the Tobacco Root Mountains, U-Pb dates from leucosomal zircon in migmatitic paragneiss and zircon in a metamorphosed mafic amphibolite dike are interpreted to record peak lower-granulite-facies metamorphism at ca. 1770 Ma (Mueller et al., 2004). A monazite U-Pb study from a variety of aluminous lithologies was alternatively interpreted to constrain prograde mineral growth from ca. 1780 Ma to peak conditions closer to ca. 1755 Ma (Cheney et al., 2004a). Continuing to the southeast in the Bear Trap Canyon area of the Northern Madison Range (Figs. 1 and 2), a deformed mafic dike records high-pressure granulite-facies metamorphism at ca. 1750 Ma (U-Pb zircon; Ault et al., 2012). Our new data from the central portion of the range are interpreted to record prograde to peak metamorphism from ca. 1750 to 1720 Ma. In summary, the younging of high-grade tectonometamorphism by at least 40 m.y., and perhaps as much as 80 m.y., extends across at least 80 km from the Highland Range to at least the central Northern Madison Range (Fig. 14). This suggests growth or migration of the hinterland of the orogen toward its foreland, where the latter is considered to be represented by substantially cooler Proterozoic temperatures (e.g., Giletti's line or modern equivalent) and discrete greenschist-grade structures like the Madison mylonite zone (Fig. 1B).

Several explanations for this spatio-temporal pattern of Paleoproterozoic metamorphism appear plausible. First, the simplest interpretation is that the observed southeastward younging of tectonism may represent synconvergent lateral growth of the metamorphic core of the orogen by in-sequence thrusting and thickening (e.g., Willett et al., 1993), caused by either protracted or episodically accelerated collision. Similar propagation patterns representing >50 m.y. of continued convergence and growth of deformation and metamorphism into the foreland are observed in other well-known major collisional belts, such as the ca. 1090–995 Ma Grenville (e.g., Jamieson et al., 1995; Hynes and Rivers, 2010), the 55 Ma to present Himalayan (e.g., Hodges, 2000) orogens, and Jurassic to Early Cretaceous foreland-directed growth of the northern Canadian Cordilleran hinterland (Staples et al., 2014). Alternatively, synconvergent thickening of the core of the Big Sky orogen may have been followed by postconvergent shortening and associated metamorphism from thickening on the flanks of the mountain belt driven by gravitational spreading. This phenomenon is observed in numerical models and was invoked by Jamieson and Beaumont (2011) to explain the synconvergent Ottowan phase (1090–1020 Ma) of high-grade metamorphism in the core of the Grenville orogen versus the later Rigolet phase (1005–995 Ma) of thrusting and medium-grade metamorphism in the Grenville front tectonic zone. Other possibilities include one or a combination of additional tectonic processes that could have resulted in juxtaposition of domains with older and younger tectonometamorphic signatures, such as gneiss dome formation, channel flow, or later strike-slip displacements. Given our current understanding of the Big Sky orogeny, we lack clear constraints on which of these models is most plausible. Each of these scenarios could be tested through further structural and geochronological studies. For instance, expanding our current understanding of the poorly constrained high-strain zones within the Northern Madison Range may yield potential constraints on one or more of these models.

Our results suggest a systematic pattern in the age of peak metamorphism from northwest to southeast, but subsequent cooling histories and exhumation patterns are less well constrained. Several studies have reported ca. 1.8–1.7 Ga $^{40}Ar/^{39}Ar$ hornblende and biotite cooling dates, generally corroborating earlier work by Giletti (1966), although no $^{40}Ar/^{39}Ar$ data exist yet from the Northern Madison Range. Harlan et al. (1996) reported ca. 1.80 Ga $^{40}Ar/^{39}Ar$ dates from the Highland Mountains. A large $^{40}Ar/^{39}Ar$ data set from the Highland, Ruby, and Tobacco Roots Mountains yielded a mean of ca. 1.76 Ga (Roberts et al., 2002). Both of these results are older than the interpreted timing of peak metamorphism in the central Northern Madison Range (Figs. 1, 2, and 14), suggesting that these rocks had cooled through 300 °C and been exhumed prior to the time when other portions of the orogen experienced their peak conditions. However, a second and equally large thermochronology data set from the Ruby and Tobacco Root Mountains suggests significantly younger and rapid ca. 1.71 Ga cooling through the 500–300 °C temperature interval (Brady et al., 2004a). This is also supported by the youngest monazite (ca. 1730–1713 Ma) from the Tobacco Root Mountains, which is interpreted to have grown during retrograde decompression (Cheney et al., 2004). The youngest dates in that study (1713 Ma) are similar to those in this study (ca. 1705 Ma) in the Northern Madison Range, which is also interpreted to be related to garnet breakdown during exhumation. In summary, both differential and simultaneous exhumation may have occurred across different parts of the region, but more work is needed to clarify this history.

Significant uncertainty remains regarding how the kinematics of deformation varied spatially and temporally across the region. For example, Mueller et al. (2005) and Foster et al. (2006) pointed out that magmatism and associated metamorphism occurred almost 100 m.y. earlier in the Little Belt Mountains (ca. 1.86–1.81 Ga) than in southwest Montana, and they used this to suggest that the Big Sky orogeny may be a distinctly younger and separate collisional event. They envisioned an early orthogonal 1.9–1.8 Ga collision event, associated with suturing of the Archean Medicine Hat and Wyoming cratons (Great Falls tectonic zone), evolving to convergence with a stronger transpressional component associated with accretion of a separate Paleoproterozoic terrane during the Big Sky orogeny (e.g., Selway terrane of Foster et al., 2006). If so, a kinematic record of these transitions is likely preserved in the basement rocks of southwest Montana.

CONCLUSIONS

Spatial and temporal patterns of deformation and metamorphism yield insight into the kinematics, rheology, and overall tectonic significance of exhumed paleo-orogens, and they allow better understanding of the processes at work in active orogens of similar scales. Thermotectonism associated with the Big Sky orogeny modified much of southwest Montana from ca. 1.8 to 1.7 Ga. This contribution expands the known width of the high-grade metamorphic core of the orogen by ~40 km farther southeast across strike from the northwest end of the Northern Madison Range. Structural relationships, metamorphic petrology, and U-Pb geochronology indicate that at least two episodes of late Paleoproterozoic deformation (D_2 and D_3), including the dominantly NE-striking and moderately SE-dipping foliation and associated isoclinal folds and lineation, affected rocks in the central Northern Madison Range. Synkinematic metamorphism, recorded in both mafic dikes and pelitic schist, reached peak conditions of 0.9–0.8 GPa and ~700 °C at 1750–1720 Ma. Combined with other regional data, a pattern of southeastward younging of high-grade metamorphism by 80–40 m.y. is apparent across an ~100 km transect from the Highland Mountains through the study area. Although additional work is needed to fully fingerprint the particular tectonic mechanism(s) at play here, this pattern suggests that lateral growth of the orogenic core toward the foreland during protracted collision is likely to be an important characteristic of one of North America's most recently recognized major convergent belts.

ACKNOWLEDGMENTS

We would like to thank Katherine Barnhart, Kevin Toeneboehn, Diana Rattanasith, and Omero Orlandini for assistance in the field, and Karl Kellogg for sharing his previous mapping work from the Spanish Peaks region. Financial support for this project was provided by National Science Foundation grant EAR-1252295 to Mahan, U.S. Geological Survey EDMAP grant G12AC20182 to Mahan and Condit, and student research grants from the Geological Society of America, Rocky Mountain Association of Geologist Stone-Holberg Scholarship, Tobacco Roots Geological Society, and Colorado Scientific Society to Condit. Axel Schmitt (formerly at University of California–Los Angeles), Kevin Chamberlain (University of Wyoming), and Mike Jercinovic (University of Massachusetts) are thanked for their assistance in their respective geochronology laboratories. Tekla Harms, Paul Mueller, David Foster, and Dan Gibson are thanked for constructive reviews of earlier versions of this manuscript.

REFERENCES CITED

Alcock, J., Muller, P.D., and Jercinovic, M.J., 2013, Monazite ages and pressure-temperature-time paths from anatectites in the southern Ruby Range, Montana, USA: Evidence for delamination, ultramafic magmatism, and rapid uplift at ca. 1780 Ma: Canadian Journal of Earth Sciences, v. 50, p. 1069–1084, doi:10.1139/cjes-2013-0035.

Allaz, J.M., Williams, M.L., Jercinovic, M.J., and Donavan, J., 2011, A new technique for electron microprobe trace element analysis: The multipoint background method, *in* EMAS 2011 Book of Tutorials and Abstracts: Angers, France, Modern Developments and Applications in Microbeam Analysis, p. 319–320.

Ault, A.K., Flowers, R.M., and Mahan, K.H., 2012, Quartz shielding of sub-10 μm zircons from radiation damage–enhanced Pb loss: An example from a metamorphosed mafic dike, northwestern Wyoming craton: Earth and Planetary Science Letters, v. 339–340, p. 57–66, doi:10.1016/j.epsl.2012.04.025.

Berman, R.G., 1991, Thermobarometery using multi-equilibrium calculations: A new technique, with petrological applications: Canadian Mineralogist, v. 29, p. 833–855.

Berman, R.G., and Aranovich, L., 1996, Optimized standard state and solution properties of minerals: Contributions to Mineralogy and Petrology, v. 126, p. 1–24, doi:10.1007/s004100050232.

Berman, R.G., Aranovich, L.Y., Rancourt, D.G., and Mercier, P.H.J., 2007, Reversed phase equilibrium constraints on the stability of Mg-Fe-Al biotite: The American Mineralogist, v. 92, p. 139–150, doi:10.2138/am.2007.2051.

Boerner, D.E., Craven, J.A., Kurtz, R.D., Ross, G.M., and Jones, F.W., 1998, The Great Falls tectonic zone: Suture or intracontinental shear zone?: Canadian Journal of Earth Sciences, v. 35, p. 175–183, doi:10.1139/e97-104.

Brady, J.B., Kovaric, D.N., Cheney, J.T., Jacob, L.J., and King, J.T., 2004a, $^{40}Ar/^{39}Ar$ ages of metamorphic rocks from the Tobacco Root Mountains region, Montana, *in* Brady, J.B., Burger, H.R., Cheney, J.T., and Harms, T.A., eds., Precambrian Geology of the Tobacco Root Mountains, Montana: Geological Society of America Special Paper 377, p. 131–149.

Brady, J.B., Mohlman, H.K., Harris, C., Carmichael, S.K., Jacob, L.J., and Chaparro, W.R., 2004b, General geology and geochemistry of metamorphosed Proterozoic mafic dikes and sills, Tobacco Root Mountains, Montana, *in* Brady, J.B., Burger, H.R., Cheney, J.T., and Harms, T.A., eds., Precambrian Geology of the Tobacco Root Mountains, Montana: Geological Society of America Special Paper 377, p. 89–104.

Burger, H., Peck, W.H., Johnson, K.E., Tierney, K.A., Poulsen, C.J., Cady, P., Lowell, J., MacFarlane, W.A., Sincock, M.J., Archuleta, L.L., Pufall, A., and Cox, M.J., 2004, Geology and geochemistry of the Spuhler Peak Metamorphic Suite, *in* Brady, J.B., Burger, H.R., Cheney, J.T., and Harms, T.A., eds., Precambrian Geology of the Tobacco Root Mountains, Montana: Geological Society of America Special Paper 377, p. 47–70, doi:10.1130/0-8137-2377-9.47.

Cheney, J., Webb, A., Coath, C., and McKeegan, K., 2004a, In situ ion microprobe $^{207}Pb/^{206}Pb$ dating of monazite from Precambrian metamorphic suites, Tobacco Root Mountains, Montana: Geological Society of America. Special Paper, v. 377, p. 151–179, doi:10.1130/0-8137-2377-9.151.

Cheney, J.T., Brady, J.B., Tierney, K.A., et al., 2004b, Proterozoic metamorphism of the Tobacco Root Mountains, Montana, *in* Brady, J.B., Burger, H.R., Cheney, J.T., and Harms, T.A., eds., Precambrian Geology of the Tobacco Root Mountains, Montana: Geological Society of America Special Paper 377, p. 105–129.

Condit, C.B., Mahan, K.H., Ault, A.K., Flowers, R.M., and Johnson, J.E., 2012, Integrating petrology, structure, and geochronology to evaluate a possible crustal cross-section on the NW margin of the Wyoming Province, SW Montana: Geological Society of America Abstracts with Programs, v. 44, no. 7, p. 586.

Connolly, J.D., and Petrini, K., 2002, An automated strategy for calculation of phase diagram sections and retrieval of rock properties as a function of physical conditions: Journal of Metamorphic Geology, v. 20, p. 697–708, doi:10.1046/j.1525-1314.2002.00398.x.

Corfu, F., Hanchar, J.M., Hoskin, P.W., and Kinny, P., 2003, Atlas of zircon textures: Reviews in Mineralogy and Geochemistry, v. 53, p. 469–500, doi:10.2113/0530469.

Dumond, G., Mclean, N., Williams, M., Jercinovic, M., and Bowring, S., 2008, High-resolution dating of granite petrogenesis and deformation in a lower crustal shear zone: Athabasca granulite terrane, western Canadian Shield: Chemical Geology, v. 254, p. 175–196, doi:10.1016/j.chemgeo.2008.04.014.

Erslev, E., 1989, Precambrian geology and ductile normal faulting in the southwest corner of the Beartooth Uplift, Montana, *in* Bartholomew, M.J., Hyndman, D.W., Mogk, D.W., and Mason, R., eds., Basement Tectonics 8: Characterization and Comparison of Ancient and Mesozoic Continental Margins: Proceedings of the Eighth International Conference on Basement Tectonics: International Basement Tectonics Association Publication 8, p. 313–322.

Erslev, E., and Sutter, J., 1990, Evidence for Proterozoic mylonitization in the northwestern Wyoming Province: Geological Society of America Bulletin, v. 102, p. 1681–1694, doi:10.1130/0016-7606(1990)102<1681:EFPMIT>2.3.CO;2.

Foster, D.A., Mueller, P.A., Mogk, D.W., Wooden, J.L., and Vogl, J.J., 2006, Proterozoic evolution of the western margin of the Wyoming craton: Implications for the tectonic and magmatic evolution of the northern Rocky Mountains: Canadian Journal of Earth Sciences, v. 43, p. 1601–1619, doi:10.1139/e06-052.

Garihan, J.M., Schmidt, C.J., Young, S.W., and Williams, M.A., 1983, Geology and recurrent movement history of the Bismark–Spanish Peaks–Gardiner fault system, southwest Montana, *in* Lowell, J.D., and Gries, R., eds., Rocky Mountain Foreland Basins and Uplifts: Denver, Colorado, Rocky Mountain Association of Geologists, p. 295–314.

Gibson, H., Carr, S., Brown, R., and Hamilton, M., 2004, Correlations between chemical and age domains in monazite, and metamorphic reactions involving major pelitic phases: An integration of ID-TIMS and SHRIMP geochronology with Y-Th-U X-ray mapping: Chemical Geology, v. 211, p. 237–260, doi:10.1016/j.chemgeo.2004.06.028.

Giletti, B., 1966, Isotopic ages from southwestern Montana: Journal of Geophysical Research, v. 71, p. 4029–4036, doi:10.1029/JZ071i016p04029.

Giletti, B.J., 1971, Discordant isotopic ages and excess argon in biotites: Earth and Planetary Science Letters, v. 10, p. 157–164, doi:10.1016/0012-821X(71)90001-X.

Gorman, A., and Clowes, R., 2002, Deep probe: Imaging the roots of western North America: Canadian Journal of Earth Sciences, v. 39, p. 375–398, doi:10.1139/e01-064.

Grove, M., Jacobson, C.E., Barth, A.P., and Vucic, A., 2003, Temporal and spatial trends of Late Cretaceous–arly Tertiary underplating of Pelona and related schist beneath southern California and southwestern Arizona, *in* Johnson, S.E., Paterson, S.R., Fletcher, J.M., Girty, G.H., Kimbrough, D.L., and Martín-Barajas, A., eds., Tectonic Evolution of Northwestern Mexico and the Southwestern USA: Geological Society of America Special Paper 374, p. 391–406.

Hames, W., and Harms, T., 2013, Laser $^{40}Ar/^{39}Ar$ thermochronology of single crystals from Paleoproterozoic to Archean rocks of the northern Wyoming Province, Big Sky orogen, and Great Falls tectonic zone: Giletti's line revisited: Geological Society of America Abstracts with Programs, v. 45, no. 7, p. 223.

Harlan, S.S., Guissman, J.W., Snee, L.W., and Reynolds, R.L., 1996, Late Cretaceous remagnetization of Proterozoic mafic dikes, southern Highland Mountains, southwestern Montana: A paleomagnetic and $^{40}Ar/^{39}Ar$ study: Geological Society of America Bulletin, v. 108, p. 653–668, doi:10.1130/0016-7606(1996)108<0653:LCROPM>2.3.CO;2.

Harms, T.A., Brady, J.B., Burger, H.R., and Cheney, J.T., 2004a, Advances in the geology of the Tobacco Root Mountains, Montana, and their implications for the history of the northern Wyoming province: Geological Society of America. Special Paper, v. 377, p. 227–243.

Harms, T.A., Burger, H.R., Blednick, D.G., et al., 2004b, Character and origin of Precambrian fabrics and structures in the Tobacco Root Mountains, Montana, *in* Brady, J.B., Burger, H.R., Cheney, J.T., and Harms, T.A., eds., Precambrian Geology of the Tobacco Root Mountains, Montana: Geological Society of America Special Paper 377, p. 203–226.

Hodges, K., 2000, Tectonics of the Himalaya and southern Tibet from two perspectives: Geological Society of America Bulletin, v. 112, p. 324–350, doi:10.1130/0016-7606(2000)112<324:TOTHAS>2.0.CO;2.

Holland, T.J.B., and Powell, R., 2011, An improved and extended internally consistent thermodynamic data set for phases of petrological interest, involving a new equation of state for solids: Journal of Metamorphic Geology, v. 29, p. 333–383, doi:10.1111/j.1525-1314.2010.00923.x.

Hynes, A., and Rivers, T., 2010, Protracted continental collision—Evidence from the Grenville orogen: Canadian Journal of Earth Sciences, v. 47, p. 591–620, doi:10.1139/E10-003.

James, H., and Hedge, C., 1980, Age of the basement rocks of southwest Montana: Geological Society of America Bulletin, v. 91, p. 11–15, doi:10.1130/0016-7606(1980)91<11:AOTBRO>2.0.CO;2.

Jamieson, R., and Beaumont, C., 2011, Coeval thrusting and extension during lower crustal ductile flow—Implications for exhumation of high-grade metamorphic rocks: Journal of Metamorphic Geology, v. 29, p. 33–51, doi:10.1111/j.1525-1314.2010.00908.x.

Jamieson, R., Culshaw, N., and Corrigan, D., 1995, Northwest propagation of the Grenville orogen: Grenvillian structure and metamorphism near Key Harbour, Georgian Bay, Ontario, Canada: Journal of Metamorphic Geology, v. 13, p. 185–207, doi:10.1111/j.1525-1314.1995.tb00213.x.

Jercinovic, M., Williams, M., and Lane, E., 2008, In-situ trace element analysis of monazite and other fine-grained accessory minerals by EPMA: Chemical Geology, v. 254, p. 197–215, doi:10.1016/j.chemgeo.2008.05.016.

Johnson, J.E., West, D.P., Condit, C.B., and Mahan, K.H., 2014, Strain localization in the Spanish Creek mylonite, Northern Madison Range, southwest Montana, U.S.A.: Rocky Mountain Geology, v. 49, p. 91–114, doi:10.2113/gsrocky.49.2.91.

Kellogg, K., and Harlan, S., 2007, New ^{40}Ar/^{39}Ar age determinations and paleomagnetic results bearing on the tectonic and magmatic history of the northern Madison Range and Madison Valley region, southwestern Montana, U.S.A.: Rocky Mountain Geology, v. 42, p. 157–174, doi:10.2113/gsrocky.42.2.157.

Kellogg, K.S., and Mogk, D.W., 2009, Structural development of high-temperature mylonites in the Archean Wyoming Province, northwestern Madison Range, Montana: Rocky Mountain Geology, v. 44, p. 85–102, doi:10.2113/gsrocky.44.2.85.

Kellogg, K.S., and Williams, V. s., 2000, Geologic map of the Ennis 30′ × 60′ quadrangle, Bison and Gallatin Counties, Montana, and Park County, Wyoming: U.S. Geological Survey, Geologic Investigations serires I-2690.

Kohn, M.J., and Malloy, M.A., 2004, Formation of monazite via prograde metamorphic reactions among common silicates: Implications for age determinations: Geochimica et Cosmochimica Acta, v. 68, p. 101–113, doi:10.1016/S0016-7037(03)00258-8.

Kohn, M.J., and Spear, F., 2000, Retrograde net transfer reaction insurance for pressure-temperature estimates: Geology, v. 28, p. 1127–1130, doi:10.1130/0091-7613(2000)28<1127.

Krogh, T.E., Kamo, S.L., Hanley, T.B., Hess, D.F., Dahl, P.S., and Johnson, R.E., 2011, Geochronology and geochemistry of Precambrian gneisses, metabasites, and pegmatite from the Tobacco Root Mountains, northwestern Wyoming craton, Montana: Canadian Journal of Earth Sciences, v. 48, p. 161–185, doi:10.1139/E10-095.

Loehn, C.W., 2009, Monazite Geochronology of the Madison Mylonite Zone and Environs, Southwestern Montana: With Implications for Precambrian Thermotectonic Evolution of the Northern Wyoming Province [M.S. thesis]: Blacksburg, Virginia, Virginia Tech University, 94 p.

Mahan, K.H., Goncalves, P., Williams, M.L., and Jercinovic, M.J., 2006, Dating metamorphic reactions and fluid flow: Application to exhumation of high-*P* granulites in a crustal-scale shear zone, western Canadian Shield: Journal of Metamorphic Geology, v. 24, p. 193–217, doi:10.1111/j.1525-1314.2006.00633.x.

Miller, R., and Snoke, A., 2009, The utility of crustal cross sections in the analysis of orogenic processes in contrasting tectonic settings, *in* Miller, R., and Snoke, A., eds., Crustal Cross Sections from the Western North American Cordillera and Elsewhere: Implications for Tectonic and Petrologic Processes: Geological Society of America Special Paper 456, p. 1–38, doi:10.1130/2009.2456(01).

Mogk, D., 1992, Ductile shearing and migmatization at mid-crustal levels in an Archean high-grade gneiss belt, Northern Gallatin Range, Montana, USA: Journal of Metamorphic Geology, v. 10, p. 427–438, doi:10.1111/j.1525-1314.1992.tb00094.x.

Mogk, D., and Henry, D., 1988, Metamorphic petrology of the northern Archean Wyoming Province, southwestern Montana: Evidence for Archean collisional tectonics, *in* Ernst, W.G., ed., Metamorphism and Crustal Evolution of the Western United States: Englewood Cliffs, New Jersey, Prentice-Hall, p. 363–382.

Mogk, D.W., Mueller, P.A., and Wooden, J.L., 1992, The nature of Archean terrane boundaries: An example from the northern Wyoming Province: Precambrian Research, v. 55, p. 155–168, doi:10.1016/0301-9268(92)90020-O.

Mueller, P.A., and Cordua, W.S., 1976, Rb-Sr whole rocks ages of gneiss from the Horse Creek area, Tobacco Root Mountains, Montana: Isochron/West, v. 16, p. 33–36.

Mueller, P.A., and Frost, C.D., 2006, The Wyoming Province: A distinctive Archean craton in Laurentian North America: Canadian Journal of Earth Sciences, v. 43, p. 1391–1397, doi:10.1139/e06-075.

Mueller, P.A., Shuster, R.D., Wooden, J.L., Erlsev, E.A., and Bowes, D.R., 1993, Age and composition of Archean crystalline rocks from the Southern Madison Range, Montana: Implications for crustal evolution in the Wyoming craton: Geological Society of America Bulletin, v. 105, p. 437–446, doi:10.1130/0016-7606(1993)105<0437:AACOAC>2.3.CO;2.

Mueller, P.A., Wooden, J.L., Mogk, D.W., Nutman, A.P., and Williams, I.S., 1996, Extended history of a 3.5 Ga trondhjemitic gneiss, Wyoming Province, USA: Evidence from U-Pb systematics in zircon: Precambrian Research, v. 78, p. 41–52, doi:10.1016/0301-9268(95)00067-4.

Mueller, P.A., Heatherington, A.L., Kelly, D.M., Wooden, J.L., and Mogk, D.W., 2002, Paleoproterozoic crust within the Great Falls tectonic zone: Implications for the assembly of southern Laurentia: Geology, v. 30, p. 127–130, doi:10.1130/0091-7613(2002)030<0127:PCWTGF>2.0.CO;2.

Mueller, P.A., Burger, H.R., Wooden, J.L., Heatherington, A.L., Mogk, D.W., and D'Arcy, K., 2004, Age and evolution of the Precambrian crust of the Tobacco Root Mountains, Montana, *in* Brady, J.B., Burger, H.R., Cheney, J.T., and Harms, T.A., eds., Precambrian Geology of the Tobacco Root Mountains, Montana: Geological Society of America Special Paper 377, p. 181–202.

Mueller, P.A., Burger, H.R., Wooden, J.L., Brady, J.B., Cheney, J.T., Harms, T.A., Heatherington, A.L., and Mogk, D.W., 2005, Paleoproterozoic metamorphism in the northern Wyoming Province: Implications for the assembly of Laurentia: The Journal of Geology, v. 113, p. 169–179, doi:10.1086/427667.

Mueller, P.A., Wooden, J.L., Mogk, D.W., and Foster, D.A., 2011, Paleoproterozoic evolution of the Farmington zone: Implications for terrane accretion in southwestern Laurentia: Lithosphere, v. 3, p. 401–408, doi: 10.1130/L161.1.

O'Neill, J., 1998, The Great Falls tectonic zone, Montana-Idaho: An early Proterozoic collisional orogen beneath and south of the Belt Basin, *in* Belt Symposium III, v. 112, p. 222–228.

O'Neill, J., and Lopez, D., 1985, Character and regional significance of Great Falls tectonic zone, east-central Idaho and west-central Montana: American Association of Petroleum Geologists Bulletin, v. 69, p. 437–447.

O'Neill, J.M., Duncan, M.S., and Zartman, R.E., 1988, An early Proterozoic gneiss dome in the Highland Mountains, southwestern Montana, *in* Lewis, S.E., and Berg, R.B., eds., Precambrian and Mesozoic plate margins: Montana, Idaho, and Wyoming, with field guides for the 8th International conference on Basement Tectonics: Montana Bureau of Mine and Geology Special Publication 96, p. 81–88.

Paces, J.B., and Miller, J.D., 1993, Precise U-Pb ages of Duluth complex and related mafic intrusions, northeastern Minnesota: Geochronological insights to physical, petrogenetic, paleomagnetic and tectonomagmatic processes associated with 1.1 Ga Midcontinent Rift system: Journal of Geophysical Research, v. 98, p. 13,997–14,013, doi:10.1029/93JB01159.

Percival, J.A., Fountain, D.M., and Salisbury, M.H., 1992, Exposed crustal cross sections as windows into the lower crust: Continental Lower Crust, v. 23, p. 317–361.

Pyle, J.M., Spear, F.S., Rudnick, R.L., and McDonough, W.F., 2001, Monazite-xenotime-garnet equilibrium in metapelites and a new monazite-garnet thermometer: Journal of Petrology, v. 42, p. 2083–2107, doi:10.1093/petrology/42.11.2083.

Reid, H.R., McMannis, W.J., and Palmquist, J.C., 1975, Precambrian Geology of North Snowy Block, Beartooth Mountains, Montana: Geological Society of America Special Paper 157, 135 p., doi:10.1130/SPE157-p1.

Roberts, H., Dahl, P., Kelley, S., and Frei, R., 2002, New ^{207}Pb-^{206}Pb and ^{40}Ar-^{39}Ar ages from SW Montana, USA: Constraints on the Proterozoic and Archæan tectonic and depositional history of the Wyoming Province: Precambrian Research, v. 117, p. 119–143, doi:10.1016/S0301-9268(02)00076-1.

Salt, K.J., 1987, Archean Geology of the Spanish Peaks Area, Southwestern Montana [M.S. thesis]: Bozeman, Montana, Montana State University, 81 p.

Schmitt, A.K., Chamberlain, K.R., Swapp, S.M., and Harrison, T.M., 2010, In situ U-Pb dating of micro-baddeleyite by secondary ion mass spectrometry: Chemical Geology, v. 269, p. 386–395, doi:10.1016/j.chemgeo.2009.10.013.

Schumacher, J.C., 1991, Empirical ferric iron corrections: Necessity, assumptions, and effects on selected geothermobarometers: Mineralogical Magazine, v. 55, p. 3–18, doi:10.1180/minmag.1991.055.378.02.

Spear, F.S., and Pyle, J.M., 2010, Theoretical modeling of monazite growth in a low-Ca metapelite: Chemical Geology, v. 273, p. 111–119, doi:10.1016/j.chemgeo.2010.02.016.

Spencer, E., and Kozak, S., 1975, Precambrian evolution of the Spanish Peaks area, Montana: Geological Society of America Bulletin, v. 86, p. 785–792, doi:10.1130/0016-7606(1975)86<785:PEOTSP>2.0.CO;2.

Staples, R.D., Murphy, D.C., Gibson, H.D., Colpron, M., Berman, R.G., and Ryan, J.J., 2014, Middle Jurassic to earliest Cretaceous mid-crustal tectono-metamorphism in the northern Canadian Cordillera: Recording foreland-directed migration of an orogenic front: Geological Society of America Bulletin, v. 126, p. 1511–1530, doi:10.1130/B31037.1.

Tracy, R.J., Robinson, P., and Thompson, A.B., 1976, Garnet composition and zoning in the determination of temperature and pressure of metamorphism, central Massachusetts: The American Mineralogist, v. 61, p. 762–775.

Vogl, J., Foster, D., Mueller, P., Wooden, J., and Mogk, D., 2004, Lithology and age of pre-belt Precambrian basement in the Little Belt Mountains, Montana: Implications for the role of the Great Galls tectonic zone in the Paleoproterozoic assembly of North America: Northwest Geology, v. 33, p. 15–34.

Vuke, S.M., 2013, Geologic Map of the Fan Mountain, Lone Mountain, and Gallatin Peak 7.5′ quadrangles, Madison Range, Madison and Gallatin Counties, Montana: Butte, Montana Bureau of Mines and Geology Open-File Report 633, 27 p., 1 sheet, scale 1:24,000.

Weyand, E.L., 1989, U-Pb Zircon Geochronology of Archean Rocks from the Spanish Peaks Area, Madison Range, Montana [M.S. thesis]: University of Florida, 113 p.

Whitney, D.L., and Evans, B.W., 2010, Abbreviations for names of rock-forming minerals: The American Mineralogist, v. 95, p. 185–187, doi:10.2138/am.2010.3371.

Wiedenbeck, M., Alle, P., Corfu, F., Griffin, W.L., Meier, M., Oberli, F., Von Quadt, A., Roddick, J.C., and Speigel, W., 1995, 3 natural zircon standards for U-Th-Pb, Lu-Hf, trace-element and REE analyses: Geostandards Newsletter, v. 19, p. 1–23, doi:10.1111/j.1751-908X.1995.tb00147.x.

Willett, S., Beaumont, C., Fullsack, P., and Willett, S., 1993, Mechanical model for the tectonics of doubly vergent compressional orogens: Geology, v. 21, p. 371–374, doi:10.1130/0091-7613(1993)021<0371:MMFTTO>2.3.CO;2.

Williams, M.L., Jercinovic, M.J., Goncalves, P., and Mahan, K., 2006, Format and philosophy for collecting, compiling, and reporting microprobe monazite ages: Chemical Geology, v. 225, p. 1–15, doi:10.1016/j.chemgeo.2005.07.024.

MANUSCRIPT RECEIVED 17 APRIL 2015
REVISED MANUSCRIPT RECEIVED 9 JULY 2015
MANUSCRIPT ACCEPTED 28 JULY 2015

Printed in the USA

Lithosphere

Foreland-directed propagation of high-grade tectonism in the deep roots of a Paleoproterozoic collisional orogen, SW Montana, USA

Cailey B. Condit, Kevin H. Mahan, Alexis K. Ault and Rebecca M. Flowers

Lithosphere 2015;7;625-645
doi: 10.1130/L460.1

Notes